

1 **A modified Vegetation Photosynthesis and Respiration Model (VPRM) for the eastern USA**
2 **and Canada, evaluated with comparison to atmospheric observations and other biospheric**
3 **models**

4

5 Sharon M. Gourdji¹, Anna Karion¹, Israel Lopez-Coto¹, Subhomoy Ghosh^{1,2}, Kim Mueller¹, Yu Zhou³, Chris
6 Williams³, Ian Baker⁴, Katharine Haynes⁴, James Whetstone¹

7

- 8 1. National Institute of Standards & Technology, Gaithersburg, MD, USA, 20899, USA
9 2. Center for Research Computing, University of Notre Dame, South Bend, IN, 46556, USA
10 3. Graduate School of Geography, Clark University, Worcester, MA, 01610, USA
11 4. Cooperative Institute for Research in the Atmosphere (CIRA), Colorado State University, Fort
12 Collins, CO, 80521, USA

13

14

15 **Key points**

- 16 1. VPRM was customized for eastern North America with a respiration model including EVI,
17 quadratic temperature and water stress factors.
- 18 2. The modified VPRM improves agreement with atmospheric CO₂ observations by increasing
19 growing season respiration.
- 20 3. The modified VPRM better explains hourly atmospheric CO₂ variability from April to October
21 compared to other models in 2016/ 2017.

22

23 **Plain Language Summary**

24 Monitoring fossil fuel emissions with atmospheric CO₂ measurements can provide an independent check
25 on bottom-up estimates and support mitigation policies by tracking emission trends over time and
26 identifying unknown sources. However, atmospheric CO₂ is influenced by anthropogenic emissions and
27 the natural carbon cycle from plants and soils, which contributes a strong hourly-varying signal in the
28 atmosphere during the growing season. Here we implement a relatively simple model of the biosphere,
29 i.e., the Vegetation Photosynthesis and Respiration Model, at high spatiotemporal resolution in eastern
30 North America. The equation describing sources to the atmosphere from respiration (i.e., “breathing”
31 from plants and decaying organic matter) is modified to make it more physiologically realistic by
32 accounting for increases in leaf respiration during summer. Model estimates are compared with output
33 from other similar biospheric models and with atmospheric CO₂ observations, and results show that the
34 new VPRM better explains CO₂ fluctuations in the atmosphere during the growing season compared to
35 other models. The model improvements shown here demonstrate promise for helping to isolate the
36 biospheric signal in atmospheric CO₂ measurements and thus improve estimation of fossil fuel emissions
37 year-round in areas with significant nearby and upwind vegetation.

38

39

40 **Abstract**

41 Increasing atmospheric CO₂ measurements in North America, especially in urban areas, may help enable
42 the development of an operational CO₂ emission monitoring system. However, isolating the fossil fuel
43 emission signal in the atmosphere requires factoring out CO₂ fluctuations due to the biosphere,
44 especially during the growing season. To help improve simulations of the biosphere, here we customize
45 the Vegetation Photosynthesis and Respiration Model (VPRM) at high-resolution for an eastern North
46 American domain, upwind of coastal cities from Washington D.C. to Boston, MA, optimizing parameters
47 using domain-specific flux tower data from 2001 to the present. We run three versions of VPRM from
48 November 2016 to October 2017 using i) annual (VPRM_{ann}) and ii) seasonal parameters (VPRM_{seas}), and
49 then iii) modifying the respiration equation to include the Enhanced Vegetation Index (EVI), a squared
50 temperature term and interactions between temperature and water stress (VPRM_{new}). VPRM flux
51 estimates are evaluated by comparison with other models (the Carnegie-Ames-Stanford Approach
52 model, or CASA, and the Simple Biosphere Model v4), and with comparison to atmospheric CO₂ mole
53 fraction data at 21 surface towers. Results show that VPRM_{new} is relatively unbiased and outperforms all
54 other models in explaining CO₂ variability from April to October, while VPRM_{ann} overestimates growing
55 season sinks by underestimating summertime respiration. Despite unknown remaining errors in
56 VPRM_{new}, and uncertainties associated with other components of the atmospheric CO₂ comparisons,
57 VPRM_{new} appears to hold promise for more effectively separating anthropogenic and biospheric signals
58 in atmospheric inversion systems in eastern North America.

59

60 **1. Introduction**

61 Carbon dioxide (CO₂) surface fluxes from the terrestrial biosphere produce a large and variable signal in
62 the atmosphere during the growing season (due to both photosynthetic uptake and ecosystem
63 respiration) that can dwarf the signal from fossil fuel emissions in biologically productive areas (Shiga et
64 al., 2014). Even in the dormant season (e.g., December to March in the northern hemisphere),
65 biospheric sources from ecosystem respiration have the same sign and an accumulated signal in the
66 atmosphere potentially as large as that from fossil fuel emission sources, especially when integrated
67 over large areas. Within cities and their suburban surroundings there is also an active biosphere year-
68 round within parks, lawns, and gardens, and from urban street trees and city-scale agriculture
69 (Buyantuyev & Wu, 2009; Golubiewski, 2006; Nowak & Crane, 2002; Raciti et al., 2014).

70 Recent efforts to estimate anthropogenic CO₂ emissions using inversion models with atmospheric
71 measurements collected in urban and suburban areas close to fossil fuel emission sources are
72 confounded by the difficulty in separating out the biospheric from the fossil fuel signal (Lauvaux et al.,
73 2021; Miller et al., 2020; Sargent et al., 2018; Shiga et al., 2014; Yadav et al., 2016). Many previous
74 inversion studies (Gurney et al., 2002; Hu et al., 2019; Rödenbeck et al., 2003) at continental and global
75 scales factored out the influence of fossil fuel emissions (assumed as well-known) from atmospheric
76 observations and then used the inversion to optimize biospheric flux estimates. However, in order to
77 estimate emissions with atmospheric inversions, the problem must be reversed by assuming biospheric
78 fluxes as known or separately estimating both biospheric and anthropogenic fluxes with additional
79 tracers like C¹⁴ (e.g., Basu et al., 2020). Regardless, any errors in biospheric CO₂ flux estimates will be
80 directly aliased onto emission estimates, and thus, a high-quality biospheric model at fine spatial and

81 temporal scales consistent with the variability of CO₂ in the atmosphere can further help to isolate the
82 emissions signal. Put another way, the better that the biospheric CO₂ signal can be modeled in the
83 atmosphere (at surface observing locations, along aircraft trajectories and/ or in total columns as seen
84 from satellites), the more statistical power that inversion models will have to adjust the emission signal
85 using observed atmospheric CO₂ mole fractions. In fact, the terrestrial biosphere is considered as one of
86 the largest sources of uncertainty in atmospheric CO₂ inversions during the growing season for the
87 North American and smaller regional domains (Feng et al., 2019a; Feng et al., 2019b; Sargent et al.,
88 2018).

89 A further complication with inversions designed to isolate the anthropogenic CO₂ signal, especially in
90 urban areas, is that biospheric CO₂ fluxes need to be appropriately modeled not just inside the specified
91 domain, but also in upwind areas outside the domain (also known as background conditions). For urban
92 areas downwind of significant vegetation (e.g., agriculture or forests), determining the background CO₂
93 contribution to observed mole fractions can be a substantial challenge (Karion et al., 2021; Lauvaux et
94 al., 2021; Sargent et al., 2018). This is exemplified by recent efforts to expand the urban and suburban
95 atmospheric CO₂ monitoring network in the Northeast Corridor (NEC) of the USA (from Washington D.C.
96 to Boston, MA; Karion et al., 2020; Lopez-Coto et al., 2017; Pitt et al., 2020; Sargent et al., 2018), given
97 that regions upwind of the NEC include the biologically productive Appalachian deciduous forests,
98 northern mixed forests and southern pine plantations, croplands in the Midwestern Corn Belt and
99 Mississippi river valley, grasslands in Kentucky and Tennessee and coastal and northern wetlands (Figure
100 1). Furthermore, the influence of background conditions vs. fluxes inside the domain is largely a
101 function of how the domain is defined. Future efforts to combine multiple urban areas into nested
102 domain inversions (with high-resolution fluxes estimated in urban areas and coarser resolution outside,
103 e.g., Schuh et al., 2019; Turner & Jacob, 2015), would increase the signal to noise inside the domain by
104 using towers with overlapping constraints and reduce the influence of background uncertainty. With
105 such a setup, it will become even more important to appropriately model the biosphere at high spatial
106 and temporal resolution in both urban and surrounding rural areas.

107 Towards these ends, we focus here on improving and evaluating biospheric models specifically for a
108 domain in the eastern USA and Canada upwind of the NEC (Figure 1). For this region, we create a
109 customized version of the Vegetation Photosynthesis and Respiration Model (VPRM; Mahadevan et al.,
110 2008) for a single year (November 2016 to October 2017), optimizing model parameters with data from
111 flux towers in and near the domain (Figure 1), and using both annual (VPRM_{ann}) and seasonally-varying
112 (VPRM_{seas}) parameters. Given the relatively simplistic respiration model in the original Mahadevan et al.
113 (2008) formulation (with a baseline value and linear temperature dependence), we also introduce a
114 modified respiration model in VPRM (i.e., VPRM_{new}) that includes additional covariates: i) a quadratic
115 temperature term, ii) a vegetation index to better capture seasonality in autotrophic respiration, and iii)
116 a water stress scaling factor and its interactions with temperature to capture drought and soil moisture
117 effects.

118 By comparing three versions of VPRM optimized for this domain, we evaluate different aspects of model
119 improvement, and identify their contributions to improved performance relative to two types of
120 observations: flux tower direct measurements of Net Ecosystem Exchange (NEE) and near-surface
121 atmospheric CO₂ mole fractions. We also evaluate VPRM in comparison to two other commonly-used
122 terrestrial biosphere models in North America: the Carnegie-Ames Stanford Approach (CASA) model
123 (Potter et al., 1993; Randerson et al., 1996; Zhou et al., 2020) and the Simple Biosphere model, version 4

124 (SiB4; Haynes et al., 2019; Sellers et al., 1986, 1996). VPRM, CASA and SiB4 represent a range of
125 biospheric modeling approaches that vary from the most empirical (VPRM) to the most process-based
126 and mechanistic (SiB4), with the CASA model of intermediate complexity. Additional details of the
127 models and their principal differences are discussed in Section 2.1.

128 The seasonal cycles, diurnal cycles, and gridded spatial patterns of CO₂ flux estimates are first compared
129 across models, with the goal to identify differences and commonalities in model inputs, formulation and
130 outputs, and potential mechanisms contributing to differences. Next, we compare modeled fluxes to
131 flux tower NEE observations at 22 sites in the domain with relatively complete data in 2016/ 2017,
132 examining how each model's diurnal and seasonal cycle compares to observations at these discrete
133 locations. Finally, we couple modeled CO₂ fluxes with two different transport and dispersion models
134 and compare simulated atmospheric CO₂ mole fractions to measurements collected at 21 surface tower
135 locations in our domain (Figure 2). Fossil fuel emissions and background conditions are factored out to
136 isolate atmospheric CO₂ enhancements due to the biosphere, and simulations are compared to
137 observations using both monthly means and hourly time series to assess how well modeled fluxes
138 reproduce spatial gradients, seasonality and finer-scale (diurnal and synoptic) temporal variability in the
139 atmosphere. The comparison with atmospheric CO₂ measurements helps to evaluate the models using
140 a regional integrated signal (albeit with intermittent sampling in space and time and dilution due to
141 atmospheric mixing and transport), and thus identify how biological flux models manifest in reproducing
142 atmospheric CO₂ variability.

143

144 2. Methods

145 2.1 Biospheric models

146 All three biospheric models (VPRM, CASA and SiB4) separately estimate carbon release to the
147 atmosphere due to ecosystem respiration (R_e , or the sum of autotrophic, R_a , and heterotrophic, R_h ,
148 respiration) and carbon uptake due to photosynthesis (also known as Gross Primary Production, or GPP),
149 with Net Ecosystem Exchange (NEE) defined as their difference (i.e., $R_e - GPP$). Each model also
150 differentiates flux dynamics across land cover categories, referred to as Plant Functional Types (PFTs),
151 and then merges the flux estimates from each category into a total flux for each pixel. However, the
152 models differ in their physiological representations of GPP and R_e , their input datasets, PFT
153 classifications and phenology (or seasonal timing) schemes, as will be discussed further below (and
154 shown in Table S1).

155 Each biospheric model was run for a single year from Nov 1, 2016 to Oct 31, 2017 for our domain of
156 interest: -92 °W to -68 °W, 33 °N to 47 °N (Figure 1), with all models run at or downscaled to hourly
157 temporal resolution. The spatial resolution for each model varies, with VPRM run at 0.02°
158 (approximately 2 km²), CASA at 500 m in the coterminous USA (and 5 km in Canada), and SiB4 at 0.5°
159 (approximately 50 km). Flux estimates from all models are aggregated/ disaggregated to 0.1° for further
160 analysis, a scale which allows for comparison of fine-scale spatial variability and computational
161 tractability. The availability of transport model runs from two models limited the study to this single
162 year; however, weather patterns in this year were within the range of 20 years of interannual variability
163 in most parts of the domain (Figure S1).

164 In this section, we review the original VPRM model from Mahadevan et al. (2008), and then describe the
165 modified version developed for this study (Table 1). We then briefly describe the model structure and
166 implementations of CASA and SiB4 included in the model inter-comparison, with further details and
167 inputs for all three models also included in Table S1.

168

169 2.1.1 VPRM

170 The Vegetation Photosynthesis and Respiration Model (VPRM) is a diagnostic light-use efficiency model
171 that relies on remote-sensing inputs to calculate GPP and simulate phenology. It was implemented here
172 using the original equations from Mahadevan et al. (2008), as well as a version with a respiration
173 equation modified to include additional covariates, as described below. PFT-specific parameters for
174 both versions are optimized using hourly NEE observations from 69 flux towers in and near our domain
175 with data at any time from 2001 to the present (Figure 1; Table S2), excluding data in 2017 for model
176 evaluation. (More details on the flux tower data is included in the supplemental material.)

177 The GPP equation is the same for all VPRM model versions, and is defined as:

178

$$GPP = \lambda * T_{scale} * P_{scale} * W_{scale1} \frac{1}{\left(1 + \frac{PAR}{PAR_0}\right)} * PAR * EVI \quad Eq. 1$$

179

180 where PAR is Photosynthetically Active Radiation, EVI is the Enhanced Vegetation Index, and T_{scale} , P_{scale} ,
181 and W_{scale1} are temperature, phenology and water stress scaling factors, as defined in Mahadevan et al.
182 (2008). Parameters optimized with flux tower data are λ (a potential light-use efficiency factor) and
183 PAR_0 (the half-saturation constant of PAR, or photosynthetic efficiency at high light levels). $PAR * EVI$
184 represents the amount of absorbed radiation, with GPP modeled as potential uptake (i.e., $\lambda * PAR * EVI$)
185 downregulated by each of the scaling factors.

186 W_{scale1} is defined for all PFTs as:

$$W_{scale1} = \frac{1 + LSWI}{1 + LSWI_{max}} \quad Eq. 2$$

187 where LSWI is the remotely-sensed Land Surface Water Index (Chandrasekar et al., 2010) from MODIS,
188 and $LSWI_{max}$ is the site-specific maximum daily LSWI from a multi-year mean for May to October (Xiao et
189 al., 2004).

190 The original VPRM model formulation estimates R_e as a baseline value plus linear function of
191 temperature:

$$R_e = \beta + \alpha * T_{air}. \quad Eq. 3$$

192 Here, T_{air} is the surface air temperature (in °C), and β (baseline level) and α (temperature sensitivity of
193 respiration) are optimized parameters. In Mahadevan et al. (2008), T_{air} below a threshold (T_{low}) is set

194 equal to T_{low} to account for continued respiration in winter, when soils remain warmer than air
195 temperatures. Here instead, we just set predicted negative R_e values to zero.
196 For the original VPRM model, GPP (λ and PAR_0) and R_e (β and α) parameters are optimized
197 simultaneously by minimizing least squares across all 24-hours of hourly NEE observations. This
198 optimization procedure ensures zero bias on an average basis across the full time period of the data but
199 does not guarantee that optimized parameters will explain all variability, e.g. the peaks of the diurnal or
200 seasonal cycles. We first optimize a set of annual (i.e., time-invariant) parameters for each PFT, and
201 then four sets of seasonally varying parameters (for December to February, March to May, June to
202 August and September to November; Table S3), given that the optimal grouping of parameters (in time
203 and space) in VPRM remains an open question (T. W. Hilton et al., 2013, 2014). These VPRM runs using
204 the original VPRM equations are henceforth referred to as $VPRM_{ann}$ (annual parameters) and $VPRM_{seas}$
205 (seasonal parameters) throughout the paper (Table 1).

206 To help improve the respiration model, the equation for R_e is then updated to include additional
207 predictor variables:

$$R_e = \alpha_1 * T' + \alpha_2 * T'^2 + \gamma * EVI + \theta_1 * W_{scale2} + \theta_2 * W_{scale2} * T' + \theta_3 * W_{scale2} * T'^2 \quad Eq. 4$$

208 where α_1 , α_2 , γ , θ_1 , θ_2 and θ_3 are optimized parameters (discussed below), and T' are modified low
209 temperatures designed to simulate soil temperatures that remain warmer than air temperatures in
210 winter:

$$For T_{air} < T_{crit} \quad T' = (T_{air} - T_{crit}) * T_{scale} + T_{crit} \quad Eq. 5$$

$$For T_{air} \geq T_{crit} \quad T' = T_{air} \quad Eq. 6$$

211 where T_{crit} is a low temperature threshold (in °C) and T_{scale} is a scalar from 0 to 1, which is multiplied by
212 air temperatures below T_{crit} , and both are optimized parameters. This modification of low air
213 temperatures for R_e is like the fixed T_{low} threshold in Mahadevan et al (2008), but here T' can still slope
214 downward in winter. A slightly different water stress scaling factor is also used in the updated R_e
215 equation, with W_{scale2} defined as a normalized LSWI:

216

$$W_{scale2} = \frac{LSWI - LSWI_{min}}{LSWI_{max} - LSWI_{min}}. \quad Eq. 7$$

217

218 The new respiration model formulation (Equation 4) was chosen by running various multivariate
219 regressions against observed nighttime average NEE at the flux towers to determine a single equation
220 that consistently improves model fit across PFTs. Models were evaluated by comparing adjusted R^2 's
221 across different sets of potential covariates, which, like other model selection algorithms, penalizes the
222 addition of spurious predictor variables. W_{scale2} gave a slightly better model fit for the grasslands,

223 soybean/ other crops and shrubland PFTs compared to W_{scale1} , and equivalent fits for the other PFTs;
224 hence this definition of W_{scale} was chosen for the R_e equation.

225 In the modified respiration equation, the squared temperature term introduces a non-linear
226 temperature response, while EVI introduces realistic seasonality and spatial patterns into R_e estimates.
227 The W_{scale2} parameter and its interactions with temperature help to account for water stress, especially
228 at high temperatures when soils tend to dry out. Literature supports the use of these additional factors
229 to help explain R_e fluxes, given that autotrophic respiration has large seasonal increases associated with
230 canopy development (Jassal et al., 2007), current assimilation (i.e., photosynthetic uptake) is known to
231 account for a large portion of above and below-ground autotrophic respiration during the growing
232 season (Amthor, 2000; Högberg et al., 2001), and that soil moisture limits both autotrophic and
233 heterotrophic respiration during drought periods (Flexas et al., 2006; Meir et al., 2008; Molchanov,
234 2009). These additional factors have also previously been suggested as needed improvements to the
235 VPRM R_e equation in Li et al. (2020).

236 With the new R_e model, all parameters (α_1 , α_2 , γ , θ_1 , θ_2 , and θ_3) in Equation 4 are estimated as
237 coefficients from the nighttime NEE regressions using flux tower data for each PFT, while T_{crit} and T_{scale}
238 are optimized by maximizing R^2 values in the regressions across a range of realistic values. GPP
239 parameters are then optimized using partitioned daytime GPP observations (determined by subtracting
240 predicted daytime respiration from observed daytime NEE). Only one set of time-invariant parameters
241 are optimized for each PFT with this updated R_e model given that EVI and LSWI help to account for
242 seasonal changes (Table S4). This version of VPRM is henceforth referred to as VPRM_{new} (Table 1).

243 For all three versions of VPRM (VPRM_{new}, VPRM_{ann} and VPRM_{seas}), the original PFT classification from
244 Mahadevan et al. (2008) and the AmeriFlux database was re-examined to see how tower-specific
245 optimized parameters cluster across and between PFTs. Based on this preliminary analysis (Figure S2),
246 corn is separated from other crop categories, evergreen needleleaf and mixed forests are merged and
247 then divided into north and south at 40°N (the halfway latitude in the domain, where fast-growing pine
248 plantations in the south behave differently from more mature forests in boreal areas, Figure 1). This is
249 consistent with previous work (Hilton et al., 2013; J. Xiao et al., 2011) showing that stand age and
250 disturbance history may be equally as important as climate and PFTs for understanding NEE variations at
251 large regional scales. The optimal temperature for corn (which goes into the T_{scale} parameter) was set
252 higher than for other crops to match literature values and reflects higher temperature optima for C4
253 relative to C3 crops (Tables S3 and S4). Minimum, maximum and optimal temperatures for other PFTs
254 are taken from previous implementations of VPRM and based on literature values (T. W. Hilton et al.,
255 2013; Mahadevan et al., 2008).

256 For all versions of VPRM, developed land with low, medium and high intensity in the National Land
257 Cover Database (NLCD; Jin et al., 2019; Yang et al., 2018) in the USA (and “urban/ developed” in the
258 Canadian land cover product, Table S1, Figure 1) is classified as an urban PFT. However, the “developed-
259 open” category in the NLCD, i.e., cemeteries, gardens, lawns, and parks, is instead classified as
260 grasslands, with the assumption (in the absence of other information) that they behave like other
261 unmanaged grasslands. Parameters for the urban PFT are assumed to be the same as for deciduous
262 broadleaf forests (as in Hardiman et al., 2017), presumably the native vegetation of most cities in our
263 domain. A correction was then applied to reduce heterotrophic respiration (assumed as half the total)
264 by the fraction of impervious surfaces in the urban PFT, but the autotrophic respiration correction in

265 Hardiman et al (2017) was not applied, given the difficulty in identifying reference pixels outside of
266 every city in the domain. For VPRM_{new}, R_e is also lower in urban areas due to lower EVI values.
267 Gridded VPRM fluxes are estimated across the domain using the single GPP equation and two different
268 R_e equations using PFT-specific parameters, with total fluxes derived as weighted averages of PFT-
269 specific fluxes using fractional gridded land cover maps. Fluxes are estimated hourly, using daily EVI and
270 LSWI inputs (interpolated from overlapping 16-day and 8-day composite products from the MODIS Terra
271 and Aqua satellites), and hourly air temperature and radiation data from the High Resolution Rapid
272 Refresh model (HRRR; Benjamin et al., 2016). VPRM inputs, including land-cover maps, are described in
273 more detail in the supplemental material.

274

275 **2.1.2 CASA**

276 The CASA model was first developed in the 1990s to take advantage of remote-sensing data from NASA
277 satellites (Potter et al., 1993; Randerson et al., 1996) and to probe scientific questions about the global
278 carbon cycle at coarse spatial scales. Since then, it has been used extensively as a biospheric prior in
279 global and continental inversion studies, e.g. in the North American CarbonTracker CO₂ inversion system
280 from NOAA-ESRL (<https://www.esrl.noaa.gov/gmd/ccgg/carbontracker/>). CASA is a diagnostic light-use
281 efficiency model, which incorporates remotely-sensed data, meteorological inputs and light-use
282 efficiency factors to estimate GPP. Unlike VPRM, CASA also includes a process-based respiration model,
283 originally based on a simplified version of the CENTURY model (Parton et al., 1988), which tracks carbon
284 across three live pools (leaves, stems, roots), three litter pools, five soil pools and two coarse woody
285 debris pools (Zhou et al., 2020, Table S1). Respiration fluxes are then determined from each pool as a
286 function of carbon supply from photosynthetic uptake, pool-specific turnover and decay-rate constants,
287 and environmental stress factors.

288 The CASA model operates at a monthly timestep but an algorithm was introduced by Fisher et al. (2016)
289 to downscale monthly fluxes to 3-hour resolution using temperature and radiation data (further linearly
290 interpolated to an hourly resolution here). This downscaling algorithm has proven useful for inversion
291 studies that need to account for diurnal variability in biospheric fluxes in order to avoid biasing flux
292 estimates at coarser temporal and spatial scales (Gourdji et al., 2010; L. Hu et al., 2019). Even with the
293 temporal downscaling, monthly fPAR (fraction of photosynthetically active radiation) is still used to track
294 phenology in CASA, which can exacerbate phenological errors during times of rapid seasonal transitions
295 (Guindin-Garcia et al., 2012; Zhou et al., 2020). A comparison between the monthly fPAR used in CASA
296 and 8-day EVI for VPRM in cropland and deciduous broadleaf forest pixels (indicated in Figure 1) is
297 shown in Figure S3 in the supplemental material.

298 The implementation of CASA used here was run as an ensemble for the ACT-America project (Zhou et
299 al., 2020a; Zhou et al., 2020b) at relatively fine spatial scales (500 m in the coterminous US and 5 km in
300 Canada). Here, we use the Level 2 pruned version of the ensemble with 27 members, which contains
301 PFT-specific parameters calibrated with flux tower data. We then use the ensemble mean with
302 downscaled 3-hour fluxes interpolated to hourly resolution throughout the analysis. Ensemble means
303 typically have superior performance compared to individual ensemble members due to a reduction in
304 random errors (Elder, 2018; Schwalm et al., 2010). Zhou et al. (2020) also demonstrated that the CASA

305 ensemble mean included in this study agrees well with flux tower measurements compared to other
306 models, with a reasonable downscaled diurnal cycle.
307 For this study, we merge the 500 m fluxes in the US (about $\frac{1}{4}$ of land area in the domain) with the 5 km
308 resolution fluxes in Canada. Given that CASA is run using the dominant land cover in each pixel, we
309 expect that the high resolution of the 500 m runs in the USA will help to improve model performance in
310 this part of the domain by better representing patchy land covers relative to the 5 km product. Table S1
311 and Zhou et al. (2020) show other details of the CASA implementation used here.

312

313 **2.1.3 SiB4**

314 The Simple Biosphere Model (SiB), despite the name, is a complex process-based, fully prognostic model
315 of the carbon cycle which can be used to predict future carbon dynamics. Unlike CASA and VPRM, SiB
316 simulates both the carbon and energy cycles, and was originally developed for coupling with general
317 circulation models to improve their boundary conditions (Sellers et al., 1986, 1996). Like CASA,
318 respiration in SiB4 is calculated by tracking carbon pools, although with five live pools (including
319 products for agriculture) and six dead pools (two for litter, three for soil and one for coarse woody
320 debris; Table S1).

321 GPP in SiB4 is estimated using the Farquhar et al. (1980) enzyme-kinetic photosynthesis algorithm
322 (unlike CASA and VPRM) every 10 minutes, with explicit leaf and canopy-level dynamics and daily
323 updating of phenological variables and carbon pools. Thus, SiB4 has finer temporal resolution than
324 either the CASA or VPRM models. However, given the computational cost associated with running this
325 complex model with high temporal resolution, fluxes were estimated here at the spatial resolution of
326 0.5° using weighted average land-cover, which can partly account for sub-pixel variability in PFTs. The
327 weighted land-cover approach (also implemented in VPRM) has been shown to improve performance of
328 land surface models and to make model performance less sensitive to the spatial resolution of the
329 estimates (Li et al., 2013).

330 Unlike previous versions of SiB, SiB4 (Haynes et al., 2019) has prognostic phenology, with internally
331 calculated leaf area temporal dynamics. This prognostic phenology scheme has been shown to perform
332 well in croplands across distinct crop types (i.e., winter and spring wheat, corn, soybeans and generic C3
333 and C4 crops; Lokupitiya et al., 2009) and grasslands (Haynes et al., 2019), two ecosystems with sharp
334 seasonal transitions that may be difficult to detect with remote-sensing data having sparse sampling
335 frequency (Guindin-Garcia et al., 2012). However, predicted phenology can still become decoupled from
336 actual phenology due to unmodeled management effects (e.g., fertilization, irrigation, planting and
337 harvest), and other non-climatic factors such as disturbances. Table S1 shows other details of the SiB4
338 implementation used here.

339

340 **2.2 Model evaluation with observations**

341

342 In order to evaluate model performance, NEE flux estimates from the three VPRM versions, CASA and
343 SiB4 are compared to two kinds of observations: flux tower observations of NEE at 22 flux towers
344 (shown in Figure 1) and atmospheric CO₂ measurements at 21 towers in the domain (Figure 2, Table S5).

345
346 Flux towers directly measure NEE in relatively homogeneous terrain in a $\sim 1 \text{ km}^2$ footprint around each
347 tower, and thus can be used for biospheric model evaluation. Towers are selected here to have
348 relatively complete data coverage in 2016/ 2017, but still only cover only a small fraction of area in the
349 domain given the limited number of sites and their small footprint, which is not necessarily
350 representative of overall land cover patterns. However, a range of PFT's across the selected towers
351 helps to represent land cover heterogeneity in the domain, with towers sited in deciduous broadleaf
352 forest and mixed forest (6), evergreen needleleaf forest (4), wetlands (3), croplands (4) and grasslands
353 (4). Modeled NEE estimates are extracted in 2016/ 2017 at each flux tower location at the finest
354 possible spatial scale to match the flux tower footprint: 0.02° for VPRM, 500 m for CASA in the
355 coterminous USA and 5 km in Canada, and 0.5° for SiB4, but for the specific PFT of the flux tower.
356 Comparisons of flux estimates to observations across towers are principally made to assess biases in the
357 seasonal and diurnal cycles corresponding to each model. For individual towers, mismatches may occur
358 due to the spatial scale mismatch and errors in the underlying land cover maps for each model, although
359 previous work comparing regional and site-specific biospheric model runs to observations at flux tower
360 sites has found that most of the mismatch occurs because of model structure, parameters and inputs,
361 not differences in spatial scale (Raczka et al., 2013).
362
363 A complementary analysis was also performed using atmospheric CO₂ mole fractions measured at 21
364 surface towers (Figure 2, 3a; Table S5) to help evaluate biospheric model performance, as these
365 observations reflect the influence of regional CO₂ fluxes diluted by atmospheric mixing and transport.
366 The footprint (or sensitivity to fluxes in space and time) of each atmospheric observation varies by tower
367 location, inlet height and weather patterns, although the towers generally see the influence of high-
368 resolution fluxes (in space and time) near the tower, and a more diffuse signal coming from farther
369 away. With changes in wind direction and synoptic weather conditions, what towers "see" in the near-
370 field may also be sparse and variable, but on average, most parts of the domain and the full flux diurnal
371 cycle are sampled, albeit intermittently (Figure 2). Thus, atmospheric CO₂ data can help to evaluate CO₂
372 flux estimates at coarser spatial and temporal scales over more parts of the domain compared to the
373 flux tower comparison, although atmospheric measurements are not a direct measurement of CO₂ flux
374 and the comparison is subject to errors in other components (i.e., transport, background, fossil fuel
375 emissions) in the analysis, as described below.

376
377 **2.2.1 Atmospheric CO₂ tower observations, footprints and fossil fuel emission products**
378 In order to simulate atmospheric CO₂ mole fractions for comparison with observations, NEE flux
379 estimates from the models and fossil fuel emission estimates at 0.1° are multiplied by footprints from an
380 atmospheric transport model (Lin et al., 2003). This multiplication is referred to as a convolution where
381 flux units of $\mu\text{mol} * \text{m}^{-2} * \text{s}^{-1}$ are converted to $\mu\text{mol} / \text{mol}$, representing the mole fraction
382 enhancement of CO₂ at the observation location and time due to modeled fluxes in the domain. Fossil
383 fuel (FF) emissions are similarly convolved with footprints and then subtracted from CO₂ observations,
384 to remove the enhancement due to FF and isolate the biospheric influence in the atmosphere. Finally,
385 the influence of background conditions (CO₂ in air masses originating outside the domain) is also
386 subtracted from observations in order to isolate the influence of biospheric fluxes occurring solely
387 within the domain of interest. Throughout the study, we thus compare convolved NEE fluxes (or

388 simulated CO₂ enhancements) with observed biologic enhancements, defined as total observed CO₂
389 mole fractions – FF convolutions – background influence. We use the term “enhancement” here,
390 although technically these can be other positive or negative due to both biospheric sources and sinks.

391 Hourly average atmospheric CO₂ observations are used here from 21 towers in our domain (Figures 2
392 and 3, Table S5), which are primarily sited in rural areas and from a variety of data providers (Karion et
393 al., 2020; Miles et al., 2018; Mitchell et al., 2019; NOAA ESRL, 2019; Richardson et al., 2017). Other
394 potential towers were excluded from the study due to challenging topography for modeling transport or
395 urban locations where fossil fuel emissions have a stronger impact on observations. We use CO₂
396 observations at the tallest sampling inlet on each tower during afternoon hours for the analysis, with
397 “afternoon” as defined in Section 2 of the supplemental material.

398 Footprints corresponding to each atmospheric observation were generated from two different transport
399 models: WRF-STILT and NAMS-STILT. WRF (Weather Research and Forecasting model, Skamarock et al.,
400 2008) was run with a 1 km, 3 km, and 9 km nest, with the finer scale nests centered around the
401 Washington DC/ Baltimore area (Figure 2). NAMS (North American Mesoscale System; NCEI et al., 2020)
402 is a meteorological product with a spatial resolution of 12 km made publicly available by NOAA/ARL
403 ((ftp://arlftp.arlhq.noaa.gov/nams)). The Stochastic Time-Inverted Lagrangian Transport model (STILT,
404 Lin et al., 2003) was then used to generate footprints on a 0.1° grid across the domain by releasing
405 particles from each observation point and tracing them back in time and space using winds from the two
406 different meteorological products. Further details of the custom WRF runs and footprint generation is
407 included in Section 3 of the supplemental material.

408 WRF-STILT with its custom setup and higher spatial resolution may help to better model transport in the
409 Appalachian mountain range that crosses most of our domain (Pillai et al., 2011) and within the two
410 inner nests from Washington D.C. to Philadelphia, as compared to NAMS-STILT. However, without a
411 more in-depth study evaluating the two transport models in our domain, it is difficult to know which set
412 of footprints is more accurate in different regions and at different times of the year. Averaging across
413 process-based models is known to help reduce the influence of systematic and random errors (Elder,
414 2018); therefore, for this study, we average convolutions using WRF-STILT and NAMS-STILT footprints
415 and present these averaged results in the main text. Corresponding figures using convolutions from just
416 WRF-STILT or NAMS-STILT footprints alone are included in the supplemental material, and results from
417 the atmospheric CO₂ comparison are only highlighted which are robust across both transport models.

418 In order to remove the influence of fossil fuel emissions from atmospheric CO₂ observations, we pre-
419 subtract convolved fossil fuel flux estimates from the Vulcan 3.0 product (Gurney et al., 2020) in the USA
420 merged with the FFDAS product (Asefi-Najafabady et al., 2014) in Canada. Both products are defined
421 hourly for the year 2015, with FFDAS at 0.1° and Vulcan 3.0 at 1 km resolution. The merged fossil fuel
422 product at 0.1° is adjusted to match the days of week in our year of interest (2016/ 2017), given that
423 fossil fuel emissions are known to behave differently on weekdays vs. weekends (Gurney et al., 2020).

424 Uncertainty associated with fossil fuel emission estimates is generally considered to be lower than that
425 from biospheric flux estimates (Lauvaux et al., 2021), especially during the growing season; however,
426 emission magnitudes and their fine spatiotemporal patterns are not perfectly known, especially if the
427 emission product was developed for a year other than the one of interest, as in this study. In order to
428 simplify the analysis, we pick what we consider to be the highest-quality emission product defined at
429 fine spatiotemporal scales in our domain for the atmospheric CO₂ comparison. This choice is supported

430 by minimal differences between fossil fuel convolutions using different emission products (e.g., FFDAS in
431 the USA rather than Vulcan 3.0) compared to the spread associated with varying transport, biospheric
432 model and background conditions, as seen in other studies in eastern North America as well (e.g.,
433 Martin et al., 2019). However in winter, fossil fuel and biospheric enhancements for towers in the
434 domain are similar in magnitude and have the same sign (Figure 3c); thus small errors in the emissions
435 estimates could have a larger relative impact on the CO₂ analysis in winter months.

436

437 **2.2.2 Background conditions**

438 Atmospheric CO₂ observations at the towers are influenced by CO₂ fluxes occurring within the domain of
439 interest, as well as by air masses flowing into the domain from outside (predominantly from the west
440 and northwest in this case.) Thus, in order to factor out the “background” influence from atmospheric
441 CO₂ observations (Karion et al., 2021; Mueller et al., 2018), STILT virtual particles are traced backwards
442 from each observation location and time period to the points at which they exit the domain, and then a
443 4-dimensional CO₂ mole fraction field is sampled and averaged at those exit locations and time periods.
444 Modeled CO₂ mole fractions at exit points are taken from two optimized data assimilation products for
445 comparison: CarbonTracker v2019B (CT19B; Jacobson et al., 2020) and CarbonTracker Europe (CTE;
446 Peters et al., 2010).

447 Background conditions at the towers from the two products (CT19B and CTE) differ throughout the year,
448 with mean monthly differences ranging from 0.5 µmol/mol (or parts per million, ppm) in November and
449 December to 1.4 µmol/mol in August and 1.8 µmol/mol in September (Figure 3b), in part due to
450 differences in the underlying biospheric models used as priors in each optimization system. In fact, the
451 difference between the background conditions is larger in magnitude than the biologic enhancements
452 for about 23 % of observations in winter months (November to April) and 12 % of observations from
453 May to October, with even higher percentages in early spring (e.g., 37 % in March and 29 % in April).

454 Therefore, in order to minimize biases associated with background conditions (and better isolate the
455 influence of biospheric fluxes occurring inside the domain), we compare modeled atmospheric CO₂ at
456 the surface level (i.e., the total mole fraction, not their background contribution) from CT19B and CTE
457 and their mean to hourly afternoon observations at the tower locations in our year of interest. We then
458 visually inspect the monthly mean biases across towers to select the product with the smallest bias and
459 lowest spread (Figure S4) in each month. Only surface CO₂ is compared here, whereas many particles
460 exit the domain at higher altitudes and in the free troposphere; also, errors in CT19B or CTE fluxes inside
461 the domain could affect these model-data comparisons. However, 1) the CarbonTracker fluxes are
462 optimized with atmospheric CO₂ data and 2) systematic biases across towers are likely to be at least in
463 part influenced by background air flowing into the domain.

464 This analysis resulted in selecting CT19B in July, CTE in October and the mean of the background
465 products in all other months as “optimal”, with these monthly selections then used throughout the
466 atmospheric CO₂ comparisons. Using the mean of the two products in most months helps to cancel out
467 opposing biases, especially during the growing season, although residual biases in all months will still
468 affect the atmospheric CO₂ comparisons.

469

470 **2.2.3 Statistical metrics**

471 To compare variability in model simulations to flux tower NEE or biologic atmospheric CO₂
472 enhancements, we use the coefficient of determination (R²) and the Nash-Sutcliffe coefficient (or NSC,
473 Moriasi et al., 2007):

$$474 \quad NSC = 1 - \frac{\sum_{i=1}^n (pred_i - obs_i)^2}{\sum_{i=1}^n (obs_i - \bar{obs})^2}.$$

475 The R² is used to assess how much variability in the observations (obs_i) can be explained by model
476 predictions (pred_i), after accounting for any biases. The NSC is calculated using the same equation as a
477 coefficient of determination (R²), but instead of using a fitted regression model (that is guaranteed to
478 have zero mean bias), the NSC metric uses the actual model simulations, or in this case, the NEE
479 convolutions with atmospheric footprints. Therefore, the NSC can vary from -∞ to 1, with values < 0
480 indicating that the model performs worse than the observational mean for prediction (due to biases in
481 the model), and values > 0 implying a better fit than the mean. Thus, this metric allows us to assess
482 variability, while also penalizing model fits that have particularly biased flux estimates. We also include
483 comparisons between hourly convolutions and observations using other statistical metrics (like root-
484 mean squared error) by tower and season in the supplemental material.

485 **486 3. Results and discussion**
487488 **3.1 VPRM respiration model improvement**

489 The modified respiration model in VPRM_{new} (dark green points in Figures 4, S5) is shown to substantially
490 improve the fit of predicted R_e fluxes to nighttime average NEE (or R_e) observations, as compared to the
491 fit using annual (VPRM_{ann}) or seasonal (VPRM_{seas}) parameters with the original model formulation. In the
492 temperate, humid climate that covers most of our domain, including EVI was seen to be the single most
493 important factor improving model fit for VPRM_{new} across all PFTs, except in evergreen needleleaf and
494 mixed forests (Table S6). This is consistent with the fact that canopy development during the growing
495 season for crops, deciduous forests and other non-evergreen ecosystems induces large increases in
496 autotrophic respiration. In particular, the cropland PFTs (maize and soybean/ other crops) have a
497 dramatic improvement in model performance with VPRM_{new}, where e.g., the NSC in the maize PFT for
498 VPRM_{new} is 0.62 compared to 0.28 for VPRM_{seas} and 0.21 for VPRM_{ann}. In more water-limited ecosystems
499 (e.g., shrublands) and times of the year (i.e., late summer, early autumn), the water stress scaling factor
500 and its interactions with temperature also help to improve performance. For example, the NSC for
501 shrublands with VPRM_{new} is 0.33, while for VPRM_{ann} and VPRM_{seas} the NSC is negative, implying that
502 these latter models perform worse than using the observational mean for prediction.

503 In forested ecosystems, VPRM_{new} also has better performance than either VPRM_{ann} or VPRM_{seas}, but the
504 increase in NSC is less dramatic. This may be because seasonal increases in leaf area (particularly in
505 evergreen forests) and/ or water stress are relatively less important predictors of R_e fluxes in these
506 ecosystems compared to air temperature. In deciduous broadleaf forests and southern evergreen and
507 mixed forests, relatively low NSC values even with VPRM_{new} (0.33 and 0.19 respectively), may be
508 because the respiration model does not account for inputs to dead carbon pools (e.g. from leaf litter at
509 the end of the season or events like storms and logging).

510 In contrast to VPRM_{new}, night-time respiration estimates using the standard VPRM model with annual
511 parameters (i.e., VPRM_{ann}, yellow lines in Figures 4 and S5) are biased low in all PFTs at the highest
512 temperatures, as compared to historical NEE observations and to a linear regression model fit to only
513 nighttime data (purple lines). This is because the only seasonality in the original respiration model
514 comes from temperature, which is not enough to explain changes in R_e associated with seasonality in
515 biomass. Also, there is no guarantee that VPRM_{ann} will produce unbiased flux estimates for any portion
516 of the diurnal or seasonal cycle, as explained in Section 2.1.1. NSC values for VPRM_{ann} are lowest among
517 the three VPRMs across all PFTs.

518 VPRM_{seas} shows slightly higher NSC values than VPRM_{ann} for all PFTs, in part by estimating a different
519 baseline respiration in each season. In particular, the bias at high temperatures seen in VPRM_{ann} is
520 alleviated with seasonal parameters (i.e., light green lines at high temperatures in Figures 4 and S5).
521 Spring and fall show similarly positive relationships between R_e and temperature for most PFTs, but a
522 negative relationship is inferred in summer for 7 of 8 PFTs (with evergreen needleleaf and mixed forests
523 > 40°N the only exception; Table S3). This relationship apparent in the data shows that water limitations
524 play a role in limiting R_e at the height of the growing season when soil moisture has been depleted by
525 spring and early-summer growth. Nevertheless, the negative inferred relationship between
526 temperature and R_e in summer is unlikely to explain the relationship well in areas and time periods that
527 are not water-limited, and therefore provides further justification for an improved respiration model
528 that can include additional mechanistic detail.

529

530 **3.2 Gridded CO₂ flux comparison across models**

531

532 Flux estimates for GPP, R_e and NEE are first compared across the full domain by examining gridded
533 fluxes (at 0.1°) averaged across 3-monthly seasons (i.e., December/ January/ February, or DJF, March/
534 April/ May, or MAM, June/ July/ August, or JJA, and September/ October/ November, or SON). SiB4,
535 CASA and VPRM_{new} fluxes are principally compared in the main text (with corresponding plots comparing
536 VPRM_{new}, VPRM_{seas} and VPRM_{ann} in the supplemental material.) The seasonal and diurnal cycles are then
537 compared for two aggregated spatial groupings: deciduous broadleaf forest and croplands (Figure 1,
538 right panel; Figure S6). Together, these two land cover types make up about half of the land area in the
539 domain and are the predominant land covers upwind of the Northeast Corridor, thus disproportionately
540 influencing atmospheric CO₂ in many of the urbanized areas of the domain. Moreover, the Corn Belt is
541 known to be one of the most biologically productive ecosystems on Earth during the height of the
542 growing season (Gray et al., 2014; Hilton et al., 2017; Zeng et al., 2014), and therefore has a strong
543 influence on CO₂ across the domain, especially in June, July and August.

544

545 **3.2.1 GPP, R_e and NEE spatial patterns by season**

546 Gridded 3-monthly mean GPP, R_e and NEE vary across models in terms of flux magnitude and spatial
547 patterns (and with SiB4 having a coarser spatial resolution; Figures 5, 6, 7, 8, S7, S8, S9, S10). In winter
548 and spring, all the models generally capture the north-south gradient with dormant conditions in the
549 north and a more active biosphere in the south of the domain, whereas in summer and fall, the spatial
550 patterns are more distinct across models (Figure S11). Spatial patterns are, not surprisingly, influenced
551 by the underlying land cover maps for each model, such that e.g., in summer, SiB4 has a larger area of

552 peak uptake in croplands relative to the other models (Figure 7), given more extensive cropping areas in
553 Michigan, Wisconsin and the Carolinas (Figure S6). Also, CASA has strong R_e fluxes in the spring and fall
554 across large parts of the domain (Figures 6 and 8), in areas principally defined as deciduous broadleaf
555 forests, which have a larger spatial extent in this model compared to the definitions for VPRM and SiB4
556 (Figure S1). The higher R_e fluxes for CASA in spring across most parts of the domain are also related to
557 differences in timing across the models, as discussed further in Section 3.2.2.
558

559 In summer, despite differences in flux magnitude, spatial patterns for GPP, R_e and NEE fluxes are the
560 most correlated between SiB4 and VPRM_{new}, with both capturing strong net uptake in the midwestern
561 Corn Belt extending north into Wisconsin, neutral uptake in the Mississippi River valley, Alabama and
562 Georgia, and strong uptake in the northeastern USA forests (Figure 7, Figure S11). CASA also has strong
563 net uptake in cropping areas from the Corn Belt through the Mississippi River valley, but GPP is relatively
564 homogeneous throughout the domain and R_e is slightly lower in croplands compared to other areas,
565 unlike in VPRM_{new} and SiB4 which show the opposite pattern. Given that CASA and VPRM_{new} share the
566 same light-use efficiency formulation for photosynthesis, whereas SiB4 uses a more physiologically
567 realistic enzyme-kinetic formulation, the closer correspondence in GPP spatial patterns between SiB4
568 and VPRM_{new} in summer show that spatial patterns may be more influenced by the underlying land
569 cover maps, PFT-specific parameters and sub-pixel weighting in each model than the underlying
570 photosynthesis algorithm.

571
572 In addition to a larger cropland spatial extent, SiB4 fluxes also differ in timing in cropping areas
573 compared to the other models. In the Mississippi River Valley which has substantial soybean
574 production, SiB4 shows an earlier start to the cropping season in spring (Figure 6) and an earlier end in
575 summer (Figure 7). In the fall, SiB4 GPP has already shut down in all cropping areas, while R_e continues
576 at a reduced rate in the Midwestern Corn Belt, leading to large net sources from Indiana, Illinois and
577 Ohio in these months (Figure 8), consistent with results from previous atmospheric CO₂ inversions in
578 these areas (Gourdji et al., 2012). CASA and VPRM_{new} also show net sources to the atmosphere from
579 cropping areas in October and November, although lower in magnitude and less evident at the 3-
580 monthly average timescale shown here because cropland GPP in CASA extends through the end of
581 September and the VPRM respiration models do not explicitly consider inputs of dead biomass to
582 carbon pools in these months. Across the domain, SiB4 also shows the strongest R_e fluxes in the fall
583 months from forested areas in Wisconsin and Pennsylvania, whereas both CASA and VPRM show
584 stronger R_e fluxes towards the south of the domain, perhaps due to a stronger sensitivity of R_e to
585 temperature in these models.

586
587 In winter, all the models capture the north to south gradient for GPP, with non-zero productivity in the
588 south and correlations > 0.8 across models (Figure 5). Spatial patterns for winter R_e and NEE are more
589 distinct, with CASA and VPRM_{new} showing higher correlations than SiB4 and VPRM_{new} (Figure S11). In
590 this season, SiB4 shows relatively homogeneous R_e fluxes throughout the domain (as in fall), whereas
591 CASA and VPRM_{new} show reduced sources in the north compared to the south. NEE spatial patterns also
592 show opposite north-south gradients between models, with stronger net sources for SiB4 in the north of
593 the domain and for CASA and VPRM_{new} in the southern half. CASA also shows anomalously low R_e and
594 NEE fluxes in parts of Ontario during winter months, which could be related to the 5 km spatial
595 resolution (along with the dominant land cover formulation) in this part of the domain.
596

597 Across the VPRM versions, correlations in GPP spatial patterns are > 0.95 in all seasons, whereas
598 correlations in R_e spatial patterns are > 0.8, with slightly lower correlations in summer (Figures S7, S8,
599 S9, S10). VPRM_{seas} has the most distinct spatial patterns across the three versions of VPRM for R_e in
600 summer and NEE in winter, and it also shows the strongest net sources in cropping areas in the fall
601 months. Interestingly, the R_e spatial patterns for VPRM_{new} in spring, summer and fall are marginally
602 more correlated to those in CASA and SiB4 than are the correlations with VPRM_{ann} or VPRM_{seas} (Figure
603 S11), providing some evidence of improvement in skill for the new respiration model.

604
605 Finally, the three biospheric models differ in how they represent fluxes in urban areas. CASA in
606 particular shows weaker fluxes near cities (Figures 5, 6, 7, 8), e.g., in Indianapolis and Atlanta in summer,
607 given that GPP and R_e are set to zero in this model for pixels at the native spatial resolution (500 m or 5
608 km) where urban is the dominant land-cover. VPRM_{new} has somewhat lower R_e and GPP fluxes in urban
609 areas due to lower EVI and the impervious surface correction to heterotrophic respiration in this model.
610 In contrast, SiB4 does not have an urban PFT, and therefore does not show any reduced R_e or GPP fluxes
611 in pixels dominated by urban land use.

612
613 3.2.2 **GPP, R_e and NEE seasonal and diurnal cycles**

614 CASA, SiB4 and the three versions of VPRM differ in the magnitude of GPP and R_e fluxes during the
615 growing season (Figure 9) in both croplands and deciduous broadleaf forests. CASA and SiB4 have
616 similarly strong GPP at their peak in both ecosystems, and then a lower peak magnitude (by about 25%)
617 for VPRM_{new} followed by VPRM_{seas} and VPRM_{ann} (about 30 to 40% lower). GPP timing is relatively
618 consistent across the models with CASA having a slightly longer growing season, especially in croplands,
619 where the peak occurs slightly earlier in CASA and SiB4 compared to the VPRM models. R_e fluxes also
620 differ across models in terms of both magnitude and timing, with CASA having an earlier ramp-up and
621 peak (by about a month) compared to the other models, and the strongest peak magnitude, followed by
622 SiB4, VPRM_{new}, VPRM_{seas} and then VPRM_{ann}.

623 For the NEE seasonal cycle during the growing season, the models generally agree well in terms of
624 timing and magnitude in deciduous broadleaf forests, but they have more distinct patterns in croplands.
625 SiB4 has a peak NEE uptake shifted about a month earlier compared to the other models, despite a GPP
626 seasonal cycle similar in timing to CASA and a R_e seasonal cycle more similar to the VPRMs. In contrast,
627 the similarity in NEE timing between CASA and the VPRMs in croplands, despite differences in timing for
628 GPP and R_e , is likely due to some combination of both models using remote-sensing inputs and
629 calibration with flux tower NEE.

630 VPRM_{ann} and SiB4 have the strongest peak uptake in July and August in both ecosystems, and CASA and
631 VPRM_{new} the weakest (with VPRM_{seas} in the middle.) It is interesting to note that VPRM_{ann} has the
632 strongest net uptake in summer months, despite having the lowest magnitude of GPP and R_e fluxes,
633 which is because R_e in VPRM_{ann} is most depressed relative to GPP during summer months. Also, CASA
634 and SiB4 show stronger net sources to the atmosphere in winter than the VPRMs for both ecosystems,
635 given the predominance of R_e in this season.

636 The mean diurnal cycle in July for GPP and R_e (Figure S12) shows a similar pattern as that seen for the
637 seasonal cycle, i.e., CASA has the strongest component fluxes, then SiB4, followed by the three versions

638 of VPRM (with $VPRM_{new}$ stronger than $VPRM_{ann}$ and $VPRM_{seas}$). For the NEE diurnal cycle, CASA has by far
639 the strongest net afternoon drawdown and nighttime sources compared to the other models, about
640 40% stronger than SiB4 and the VPRMs, which are more similar in shape. At night in this month,
641 $VPRM_{new}$ has the second highest sources after CASA, followed by SiB4 and $VPRM_{seas}$, and then $VPRM_{ann}$.

642 Larger component fluxes for CASA and SiB4 compared to the VPRM models could be due to several
643 reasons. First, CASA and SiB4 are (mostly) neutral biosphere models that start from equilibrium carbon
644 pools in this year, which could lead to overestimation of R_e in areas with net sinks, e.g., in forests
645 recovering from disturbances (e.g. storms, insect attacks or harvest) or in croplands where harvested
646 products are transferred to other areas for consumption (Zhou et al., 2020). (As a side note, net sources
647 and sinks in VPRM primarily reflect the influence of the flux tower observations used in the parameter
648 optimization, which in this case results in a net annual sink in the domain 4.5 times greater than that for
649 CASA and SiB4 in this year.) Secondly, the flux tower observations used for VPRM parameter
650 optimization (especially at night) and/or the partitioning algorithms for separating component fluxes
651 could potentially be biased, leading to biased flux estimates (Aubinet, 2008; Lasslop et al., 2010;
652 Reichstein et al., 2005; Yi et al., 2000). Third, the parameter optimization using 24 hours of NEE data for
653 $VPRM_{seas}$ and $VPRM_{ann}$ does not ensure unbiased fluxes for any portion of the diurnal cycle, as
654 mentioned previously.

655 The differing seasonal timing in the models are also likely explained by several reasons. First, the longer
656 growing season for CASA in both GPP and R_e relative to the other models, is likely influenced by the
657 monthly fPAR inputs used to drive the model, which are coarser in time than the 8-day average EVI in
658 VPRM and daily internally-calculated Leaf Area Index in SiB4 (Figure S3; Zhou et al, 2020). Longer
659 growing seasons for process-based models compared to observations at flux towers in deciduous forests
660 was also seen in Richardson et al. (2012). The shorter growing seasons in VPRM could be more accurate,
661 but could also be influenced by long gaps in the overlapping 16-day EVI composites for each sensor, due
662 to the satellite passing too early or too late within adjacent composites (Corbin et al., 2010; Guindin-
663 Garcia et al., 2012). GPP phenology could potentially be modeled most accurately with an algorithm
664 incorporating remotely-sensed solar induced fluorescence (Joiner et al., 2011; Parazoo et al., 2019; Shiga
665 et al., 2018; X. Wang et al., 2020), which does not rely solely on “greenness” to sense growing season
666 transitions.

667 Uncertainty in the timing of R_e across models may be more difficult to diagnose, although the earlier
668 onset of R_e in CASA compared to $VPRM_{new}$ and SiB4 is also seen in Messerschmidt et al (2013), with the
669 latter timing more consistent with atmospheric column CO₂ and flux tower observations (Falge et al.,
670 2002). In future work, the timing of GPP and R_e fluxes could potentially be investigated further by using
671 additional atmospheric tracers like carbonyl sulfide measurements to separate GPP and R_e at regional
672 scales (e.g., Berry et al., 2013; Hilton et al., 2017; Wang et al., 2016). The magnitude and timing of NEE
673 across the models in this year will also be evaluated with comparison to flux tower data in Section 3.3
674 and to atmospheric CO₂ observations in Section 3.4.

675

676 **3.3 Model evaluation with flux tower observations**

677 The comparison of modeled hourly NEE to flux tower observations at 22 locations in 2016 - 2017 shows
678 that all biospheric models perform relatively well at capturing observed seasonal and diurnal variability,

679 with mean NSC values for the full year > 0.5 for most towers and models, and with CASA performing
680 marginally better at the hourly timescale than the VPRM models and SiB4, perhaps due to its finer
681 spatial scale in the USA.

682

683 Mean biases in nighttime R_e fluxes across towers (Figure 10a) are consistently different across models,
684 particularly during the height of the growing season, with VPRM_{new} relatively unbiased throughout the
685 year (albeit with a weak negative bias in June and July), VPRM_{ann} biased low from April to October, and
686 VPRM_{seas} with intermediate negative biases. The negative biases in VPRM_{ann} from June to August are
687 large relative to R_e fluxes, i.e. ~2 to 4 $\mu\text{mol/m}^2/\text{s}$ compared to a mean R_e of ~6 $\mu\text{mol/m}^2/\text{s}$ in these
688 months, while the negative biases are alleviated in VPRM_{seas} and VPRM_{new} due to higher baseline
689 summertime respiration in VPRM_{seas} and the EVI covariate in VPRM_{new} (as discussed in Section 3.1). In
690 contrast, nighttime R_e for CASA is biased high for most months of the year, particularly in April, May and
691 June, consistent with findings in Zhou et al. (2020). SiB4 R_e fluxes at night are also biased high in winter
692 from December to April, and with a large spread during the growing season but small negative biases in
693 June and July.

694

695 Mean biases in daytime NEE fluxes (Figure 10b) show a large spread across towers for each model from
696 April to November, with the three VPRM models showing similar weak source biases from June through
697 October. Although 2016/ 2017 fluxes were left out of the VPRM parameter optimization, many of the
698 same sites included in the evaluation shown here were also included in the historical optimization.
699 Thus, the daytime source biases for VPRM at the evaluation towers may be worsened by the spatial
700 scale mismatch and mixed land-cover in the full 0.02° pixel, which may be less productive overall than
701 the $\sim 1 \text{ km}^2$ flux tower footprint. CASA and SiB4 both have daytime source biases in winter months
702 (December to March), consistent with the nighttime R_e biases in these same months. CASA also shows a
703 sink bias at most towers in September and October, perhaps due to an overly extended growing season
704 in this model associated with monthly phenology based on fPAR (Figure S3; Figure S9 in Zhou et al.,
705 2020).

706 The mean diurnal cycle in July for models and observations is also shown for two specific towers: US-IB1,
707 a cropland site in Illinois growing corn in this year, and US-UMB, a deciduous broadleaf forest site in the
708 northern lower peninsula of Michigan. At US-IB1 (Figure 10c), SiB4 overestimates peak uptake in the
709 early afternoon by about 20%, whereas the VPRM models underestimate it by about 50%. CASA most
710 closely matches the magnitude and timing of daytime drawdown, albeit with a slight underestimate of
711 peak uptake. For VPRM, the spatial scale mismatch likely affects this comparison, as this 0.02° pixel is
712 only 32% corn, but also 44% other crops (which have weaker uptake), and 24% other PFT's. The CASA
713 landcover for this 500 m pixel is cropland, but CASA also parameterizes a single crop type, thus not
714 allowing for the relatively stronger uptake in some corn fields relative to soybean or other crops, which
715 is less apparent at this particular tower. At night, CASA overestimates R_e fluxes for this tower and
716 month, whereas VPRM_{new} closely matches nighttime R_e and VPRM_{seas}, VPRM_{ann} and SiB4 slightly
717 underestimate it.

718 At US-UMB (Figure 10d), the magnitude of the diurnal cycle is overestimated for CASA during both
719 nighttime and mid-day, whereas the daytime uptake for the VPRM models and SiB4 is underestimated
720 by about 20%. At night, VPRM_{new}, VPRM_{seas} and SiB4 closely match the magnitude of observed R_e ,
721 whereas VPRM_{ann} underestimates R_e by about 60%. The period of peak mid-day uptake in SiB4 is longer

722 than in the observations and the other models, thus leading to a similar total uptake during daylight
723 hours compared to the observations and more compared to the VPRM models. The spatial scale
724 mismatch could also contribute to the daytime mismatch for the VPRM models at this tower, although
725 to a lesser extent than at US-IB1, given that the 0.02° pixel surrounding US-UMB is 62% deciduous
726 broadleaf forest, but also 12% wetlands and open water.

727

728 **3.4 Model evaluation with atmospheric CO₂ observations**

729 Observed total CO₂ mole fractions (Figure 3a) and biologic enhancements (Figure 3b) show both a strong
730 seasonal cycle and a large spatial variability across towers. Mean integrated footprints summed across
731 towers in July show that most of the domain is “seen” on average by this network of towers (Figure 2,
732 left panel), with slightly less sensitivity along the edges of the domain, and stronger sensitivities in
733 summer compared to winter (when wind speeds are higher). Some towers have a stronger influence
734 from croplands (e.g., BRI, TPD, S01), wetlands (e.g., LEF, SCT), forests (e.g., AMT, DNH, HAF) or urban
735 areas (e.g., MSH, HCT), while almost all towers have some sensitivity to deciduous broadleaf forests,
736 crops and grass/pasture (including developed-open space), showing the broad influence of these land
737 covers throughout the domain (Figure 1, Table S5). The tower network is also sensitive to both day and
738 nighttime fluxes on average, with afternoon receptors typically sensitive to nearby fluxes in the morning
739 of the same day and previous night (Figure 2, right panel).

740 Simulated and observed biologic atmospheric CO₂ enhancements are compared across towers in several
741 different ways in order to evaluate both bias and variability. First, we compare weekly mean
742 enhancements throughout the year at two specific towers, with one predominantly influenced by
743 croplands (S01 in Indiana) and the other by deciduous and mixed forests (DNH in New Hampshire), the
744 two predominant land covers in the domain upwind of the NEC (Figure 1; Table S5). Then, monthly
745 mean biases are examined across all towers to see how errors in the biospheric models (in terms of
746 phenology, flux magnitudes and spatial patterns) translate into biased CO₂ across the domain and
747 throughout the year. Next, we compare hourly variability in the afternoon enhancements across towers
748 within each month, which tests the biospheric models’ ability to match the diurnal cycle, synoptic
749 variability, sub-monthly seasonality and spatial gradients seen in the observations at discrete time
750 periods. These analyses are meant to inform how incorrect representations in the biospheric models
751 would affect inversions estimating fossil fuel emissions, with biased biospheric flux estimates translating
752 directly into biased emission estimates at averaged scales, and incorrect fine-scale variability (both
753 spatial and temporal) leading to emission estimates incorrectly attributed in space and time.

754

755 **3.4.1 Weekly mean comparison at S01 and DNH**

756 Observed weekly mean biologic CO₂ enhancements at the S01 (Indiana) and DNH (New Hampshire)
757 towers show net uptake from the atmosphere from May through October (Figure 11), and net releases
758 in the rest of the year. At the S01 tower, which samples CO₂ from upwind crops, observations show a
759 narrow and strong peak drawdown briefly reaching -19 µmol/mol for one week in mid-July, whereas at
760 DNH, influenced primarily by deciduous and mixed forests (Table S5), observations show a longer period
761 of peak uptake (about 2 months in June and July) which only reaches ~-8 µmol/mol. All biospheric

762 models (CASA, SiB4 and VPRM_{new}) capture the broad seasonality seen in the observations, although with
763 differences in timing and magnitude.

764 At S01, all models perform reasonably well during the growing season in matching weekly variability,
765 with VPRM_{new} having a slightly higher adjusted R² compared to the other models (i.e., 0.82 compared to
766 0.78 for CASA and 0.73 for SiB4). SiB4 best captures the peak drawdown in July with averaged WRF and
767 NAMS-STILT convolutions and WRF-STILT alone but is too strong with NAMS-STILT convolutions (Figure
768 11a, Figure S13). The SiB4 convolutions also match the timing of the observed drawdown well in May,
769 June and July, but are too weak in August and September, and transition to a net source a couple weeks
770 early compared to observations in the fall. For CASA and VPRM_{new}, the growing season drawdown starts
771 a few weeks late in June, but both models match the observed timing well from August into September.
772 In the dormant season from November to April, SiB4 modeled enhancements show the closest
773 correspondence to observations in terms of both the NSC and adjusted R² (Figure 11, left panel).

774 At DNH, VPRM_{new} better explains weekly variability during the growing season substantially compared to
775 the other models (with an adjusted R² of 0.80 for VPRM_{new}, compared to 0.55 and 0.50 for CASA and
776 SiB4). In the winter months, SiB4 best captures the weekly variability (adjusted R² of 0.47 compared to
777 0.30 for VPRM_{new} and 0.13 for CASA) although with the lowest NSC values due to flux estimates which
778 are biased high (Figure 11b). Both CASA and SiB4 start the growing season slightly late in May and end
779 the growing season too late in September and October compared to observations, whereas VPRM_{new}
780 matches the timing of the observations much more closely in these seasonal transition months. In June
781 and July, VPRM_{new} and SiB4 have too much net uptake compared to observations, although the
782 magnitude of peak uptake is sensitive to which transport model is used (Figure S14). At DNH, NAMS-
783 STILT transport makes all biospheric models look more biased in June and July, perhaps pointing to
784 errors in summertime footprint strength upwind of this tower. In general, the summertime biases in the
785 biospheric models at both S01 and DNH are sensitive to transport, demonstrating, as in Feng et al.
786 (2019), that transport model uncertainty tends to amplify biospheric model uncertainty during the
787 growing season, although biases in the dormant season for each model are also seen to be sensitive to
788 transport here.

789

790 3.4.2 Monthly mean biases across towers

791 Simulated biologic CO₂ enhancements show seasonal biases across towers and biospheric models, with
792 all three VPRMs biased low in December and January, SiB4 and CASA biased high in February and May,
793 VPRM_{ann} biased low from June to August, SiB4 and VPRM_{seas} biased low in July, and all models biased
794 somewhat low in October (Figure 12, Table 2). On the positive side, VPRM_{new} and CASA both look
795 relatively unbiased during summer months (i.e., June to August, albeit with some sensitivity to
796 transport, Figure S15), and all the VPRM versions look relatively unbiased from February to May and in
797 October and November, pointing to skill in simulating growing season transitions. SiB4 is the least
798 biased model on average across towers in December and January, although it also has the largest spread
799 in biases throughout the year, particularly in April, July and September, which could be associated with
800 its coarse spatial resolution in this study.

801 The biases in atmospheric enhancements seen here for each of the biospheric models (which could also
802 be influenced by biased transport, background and/ or fossil fuel emissions) point to weaknesses in each

803 of the biospheric model setups. First, it appears that the low bias in VPRM_{ann} in summer months is likely
804 due to not enough increase in seasonal R_e in this model, particularly at night (as seen in the flux tower
805 comparison, Figure 10), with this problem alleviated by the use of seasonal parameters in VPRM_{seas} or
806 the EVI covariate in the new respiration model (for VPRM_{new}). This result also shows the strong
807 influence of nighttime fluxes on afternoon CO₂ observations (Figure 2), given that the VPRM models
808 differ most in terms of R_e fluxes, which dominate the signal at night (Figure 9), as also seen in Hu et al.
809 (in review) and T. Lauvaux et al. (2008, 2012). The negative bias for VPRM_{seas} in July could be due to the
810 negative relationship between temperature and R_e inferred for this model setup, which unrealistically
811 lowers R_e in this month.

812 Secondly, the negative bias in flux estimates in December and January across all VPRM setups could
813 point to a bias in the flux tower nighttime NEE observations used for optimization (Barr et al., 2013).
814 While systematic errors in other components of the analysis, i.e., transport, background conditions,
815 fossil fuels, cannot be ruled out, a bias in flux tower observations themselves is supported by studies
816 suggesting that drainage loss due to horizontal advection in eddy-covariance systems, particularly at
817 night with a stratified stable boundary layer, is non-negligible and represents flux to the atmosphere
818 that is not measured (Aubinet, 2008; Nicolini et al., 2018). In addition, the biases seen in the VPRM
819 enhancements in these months is evident with both sets of footprints and background conditions, as
820 well as with fossil fuel convolutions using FFDAS across the entire domain. If the problem is in fact an
821 observational bias in the flux tower data, this could point to systematic underestimation of respiration in
822 VPRM throughout the year, which would be more difficult to detect with atmospheric CO₂ in months
823 when GPP fluxes are stronger.

824 The biases in atmospheric CO₂ seen for CASA and SiB4 also have several plausible mechanisms. The
825 positive biases in February and May and for most towers in November and March (also Figure S16) are
826 likely due to over-estimated R_e in these models associated with balanced biosphere assumptions which
827 do not account for vegetative and soil carbon sinks (Haynes et al., 2019; Zhou et al., 2020). Similarly,
828 Zhou et al. (2020) also found an NEE source bias in the CASA ensemble mean compared to flux tower
829 data from November to March in all biome types. The biases in May and October for SiB4 and CASA also
830 point to difficulties in simulating phenology during seasonal transition months, but potentially also
831 errors in the relative extent of crops and forests in each model (Figure S6), given that these two land
832 cover types have different timings of seasonal drawdown (Figure 9). Difficulty simulating autumn
833 phenological transitions in these two process-based models, particularly in deciduous forest ecosystems
834 (e.g., near DNH), is also consistent with results from the model inter-comparison study of Richardson et
835 al. (2012).

836 For SiB4, the biases in July, August and September are especially strong for the three towers with large
837 cropland influence (Figure S16; Table S5), i.e., TPD and BRI, with negative biases in July of -5 μmol/mol
838 and -7 μmol/mol respectively, and S01, with positive biases of 4 μmol/mol in August and September.
839 This could point to errors in cropland fluxes for SiB4 associated with an over-estimate of the uptake rate,
840 the prognostic phenology and/ or their spatial extent (Figure 7, Figure S6). These errors then propagate
841 throughout the domain, given that all towers have some amount of cropland influence in their
842 footprints (Table S5) due to the horizontal advection of air masses towards the east of the domain.
843 CASA and VPRM_{new} also show anomalous behavior at these same towers during summer months, which
844 points to the difficulty in accurately simulating the strong drawdown in the Corn Belt for crop PFTs
845 across models.

846

847 **3.4.3 Comparison of hourly CO₂ variability across towers**

848 The hourly comparisons of simulated to observed biologic CO₂ enhancements across towers by month
 849 show that VPRM_{new} generally outperforms all other models in reproducing CO₂ variability during the
 850 growing season in terms of both NSC's and R²s, with an average NSC from May to October of 0.38
 851 compared to 0.32 for VPRM_{seas}, 0.25 for VPRM_{ann}, 0.24 for CASA, and 0.05 for SiB4 (Figures 13, S17).
 852 Tower-specific RMSE, NSC and R² metrics calculated with hourly enhancements (Tables S7, S8, S9, S10)
 853 are also highest for VPRM_{new} at most towers in the spring, summer and fall, and even in winter with the
 854 R² metric, although CASA is least biased in this season.

855 All three versions of VPRM also have significantly higher R² values compared to CASA and SiB4 in May,
 856 June, September and October, and higher NSC values in May, September and October (due to the
 857 summer-time sink biases in VPRM_{ann}). This result points to strengths in VPRM across versions associated
 858 with the high temporal resolution phenology and potentially the domain-specific parameter
 859 optimization for this study, and not just the improved R_e model in VPRM_{new}. In the winter months,
 860 performance across the VPRM versions and CASA is more equivalent, with some month-to-month
 861 variation, and SiB4 again showing the lowest correspondence with observations. For SiB4, NSC values
 862 are negative in February, April, July, September and October and R²s are < 0.1 in April, September and
 863 October, pointing to problems simulating phenology and high-resolution spatial variability in this model,
 864 as well as having biased flux estimates, e.g., in July. CASA NSC values are positive for all months of the
 865 year except February.

866 For all biospheric models, the NSC and adjusted R² metrics are somewhat higher during the growing
 867 season from May to October when the biospheric signal is stronger (Figures 3b, 3d), compared to winter
 868 months (November to February), when the uncertainties associated with transport, fossil fuel emissions
 869 and background become proportionally larger due to weaker biologic enhancements. In fact, the mean
 870 biologic enhancements in January across towers are of similar magnitude to the fossil fuel emission
 871 enhancements (Figure 3c), given the large extent of the domain over which R_e fluxes accumulate in the
 872 atmosphere. The biospheric models also better explain hourly variability in atmospheric CO₂ when
 873 biases are accounted for, as seen by higher R² values across months compared to NSC values (Figure 13).
 874 However, NSC and adjusted R² values are no higher than 0.4 and 0.5 respectively in any month
 875 throughout the year, pointing to substantial unexplained variability in modeled CO₂ compared to
 876 observations. The unexplained variability could be due to errors in biospheric flux estimates, but also
 877 from errors in transport, boundary conditions and/ or fossil fuel emissions.

878 Interestingly, the NSC and adjusted R² metrics are higher when using averaged WRF-STILT and NAMS-
 879 STILT convolutions, compared to using either transport model alone (Figure S17); e.g., the mean
 880 VPRM_{new} NSC from May to October goes up to 0.38 with mean transport convolutions compared to 0.33
 881 with WRF-STILT and 0.29 with NAMS-STILT transport alone, and up to 0.13 with the mean convolutions
 882 from November to April, compared to 0.05 using WRF-STILT and NAMS-STILT footprints alone. This
 883 suggests that convolution averaging helps to reduce random errors and potentially cancel out some
 884 biases in the transport simulations. NSC values calculated using NAMS-STILT in general are lower during
 885 the growing season compared to the metrics with WRF-STILT for all biospheric models (Figure S17),
 886 which points to potential biases in footprint strength in NAMS-STILT during these months, as also seen
 887 in the CO₂ comparison at DNH.

888

889 **4. Conclusions, future work and recommendations**

890 Three versions of VPRM were run for this study in a single year from November 2016 to October 2017
891 using customized parameters for an eastern North American domain: i) the original Mahadevan et al.
892 (2008) implementation with annual parameters ($VPRM_{ann}$), ii) the same model formulation with
893 seasonally-varying parameters ($VPRM_{seas}$), and iii) a modified respiration model that accounts for
894 seasonality in biomass and water stress ($VPRM_{new}$). Flux estimates from the three VPRM versions were
895 compared to flux tower observations and atmospheric CO₂ observations at 21 towers across the
896 domain, and with flux estimates from the CASA and SiB4 biospheric models in this year.

897 Results show that the new respiration model in $VPRM_{new}$ increases the magnitude of nighttime R_e fluxes
898 during the growing season, and thereby helps to realistically strengthen the diurnal and seasonal cycles
899 of NEE compared to using the original respiration model which has a baseline value and a simple linear
900 function of temperature. $VPRM_{new}$ thus better reproduces spatiotemporal variability in hourly
901 atmospheric CO₂ observations, in part due to the strong influence of nighttime fluxes on afternoon CO₂
902 enhancements. In contrast, using annual parameters with the original VPRM model is seen to
903 underestimate R_e during the height of the growing season, which results in a sink bias relative to
904 atmospheric observations in these months. Using seasonal parameters removes the summertime bias
905 but also puts an unrealistic negative relationship between temperature and R_e for 7 of 8 PFTs in this
906 season.

907 The inter-comparison of the VPRMs with SiB4 and CASA sheds some light on the relative strengths and
908 weaknesses of each model, at least as seen in this single year. Overall, $VPRM_{new}$ and $VPRM_{seas}$ are less
909 biased and better explain the variability in hourly atmospheric CO₂ during the growing season compared
910 to CASA and SiB4. The strong diurnal cycle in CASA NEE is seen to be somewhat overestimated
911 compared to flux tower observations during the growing season, and with R_e fluxes overestimated year-
912 round. However, CASA NEE fluxes are relatively unbiased compared to afternoon atmospheric CO₂
913 observations at the height of the growing season, although the growing season overly extended into the
914 spring and fall. SiB4 has the most mechanistic detail among the three models but does not closely
915 match observed variability in the atmosphere in this particular year. This could be because of its coarse
916 spatial resolution in this study, its prognostic phenology (with errors in the timing of either GPP or R_e), or
917 errors in the underlying land cover maps.

918 The strong performance from a careful implementation of a relatively simple model like VPRM shown
919 here suggests that some of the mechanistic detail in more complex models may not be needed to
920 represent fine spatiotemporal variability of CO₂ in the atmosphere due to the terrestrial biosphere (as
921 also found in Racza et al., 2013; Schwalm et al., 2010). Across all versions of VPRM, the custom
922 parameter optimization using domain-specific historical flux tower data, fine temporal resolution
923 observed phenology, high spatial resolution flux estimation with weighted average PFTs and high-
924 resolution met drivers all help to improve model performance. Each of these factors could help to
925 explain the improved performance of $VPRM_{new}$ relative to CASA and SiB4, with these latter models likely
926 having more realistic model structures, particularly for R_e, but coarser spatial or temporal resolutions.
927 At the height of the growing season however, none of the models explain more than 50% of the
928 variability in atmospheric observations, which could be due to errors in modeled transport, background
929 conditions, or fossil fuel estimates, but also due to errors in NEE estimates across biospheric models.

930 Potential future improvements to VPRM include i) incorporating SIF into the GPP equation (e.g., Luus &
931 Lin, 2015; Turner et al., 2020a) to better simulate growing season transitions and water stress (when
932 CO₂ uptake can become decoupled from “greenness” observed by satellites), ii) further modifying the
933 respiration equation to incorporate accumulated EVI and/ or simultaneous GPP (to represent biomass,
934 as in Xiao et al., 2011 and to account for the large contribution of recently assimilated carbon to
935 autotrophic respiration), disturbance maps (to potentially improve spatial patterns), and week-to-week
936 changes in EVI to account for inputs to surface litter pools at the end of the growing season, and iii)
937 using pre-partitioned GPP and respiration data in the parameter optimization with more sophisticated
938 algorithms for separating component fluxes, thus improving simulation of the flux diurnal cycle. In
939 addition, the siting of new flux towers, especially in the southern half of the domain, in urban areas and
940 across disturbance gradients, would help to improve the representativeness of optimized model
941 parameters and flux estimates (as well as for CASA which also uses flux tower data for parameter
942 calibration).

943 Along with parallel and continuing development for each biospheric model, the results of this study
944 point towards what we might need in an “optimal” biospheric model for use in high-resolution CO₂
945 inversions in eastern North America, whether the biospheric signal is pre-subtracted from atmospheric
946 observations or the inversion setup allows for the estimation of fossil fuel and biospheric fluxes
947 simultaneously. Such a model should ideally include some or all of the following items: multiple land
948 covers within each pixel weighted by fractional coverage or else very high spatial resolution (e.g., less
949 than 100 m x 100 m), separation of different crop types to account for the strong uptake of corn relative
950 to other crops, sub-monthly diagnostic phenology using EVI or SIF to better account for uptake during
951 early and late growing-season transitions and water-stressed periods, more accurate land cover maps,
952 improved mechanistic representation of R_e fluxes, perhaps aided by remote-sensing inputs, and the
953 inclusion of processes allowing for net annual vegetative and soil sinks in models that track carbon
954 pools. Future work using the tower CO₂ data in an atmospheric inversion model will also help to further
955 identify needed improvements in the biospheric models that will help to enable an operational
956 atmospheric emission monitoring system in North America.

957 **Acknowledgements**

958 The authors thanks Hratch Semerjian and David Allen (NIST) for their review and advice on the
959 manuscript. This work was partially funded by NIST's Greenhouse Gas Measurements Program. Chris
960 Williams and Yu Zhou were funded by NASA award #NNX16AN17G from the Atmospheric Carbon and
961 Transport (ACT) - America project of the NASA Earth Venture Suborbital 2 program. Ian Baker was
962 supported by NASA ACT-America subcontract 80NSSC20K0924. Funding for AmeriFlux data resources
963 was provided by the U.S. Department of Energy's Office of Science.

964 SMG conceived of the study, ran VPRM, analyzed results and wrote the paper. ILC generated the
965 footprints and provided initial model code for the gridded VPRM runs. AK generated the background
966 conditions. YZ and CW provided the CASA model runs, while KH and IB provided the SiB4 runs. All co-
967 authors gave ideas for analysis and helped edit the paper.

968

969 **Data availability**

970 Scripts to generate the results shown here, along with input data and summary files, are archived on the
971 NIST server data.nist.gov at [doi:10.18434/mds2-2362](https://doi.org/10.18434/mds2-2362). DOIs for other datasets used in the paper are
972 listed below.

973

974 *Atmospheric CO₂ data:*

975 Karion, Anna, Prinzivalli, Steve, Fain, Clayton, Stock, Michael, DiGangi, Elizabeth, Biggs, Bryan,
976 Draper, Charlie, Baldelli, Seth, Veseshta, Uran, Salameh, Peter, Callahan, William, Whetstone,
977 James (2019), Observations of CO₂, CH₄, and CO mole fractions from the NIST Northeast Corridor
978 urban testbed, National Institute of Standards and
979 Technology, <https://doi.org/10.18434/M32126> (Accessed 2020-12-23)

980

981 *Flux tower data:*

982 Arain, M. Altaf (2003-) AmeriFlux CA-TP1 Ontario - Turkey Point 2002 Plantation White Pine, Dataset.
983 <https://doi.org/10.17190/AMF/1246009>
984 Arain, M. Altaf (2003-) AmeriFlux CA-TP3 Ontario - Turkey Point 1974 Plantation White Pine, Dataset.
985 <https://doi.org/10.17190/AMF/1246011>
986 Arain, M. Altaf (2012-) AmeriFlux CA-TD Ontario - Turkey Point Mature Deciduous, Dataset.
987 <https://doi.org/10.17190/AMF/1246152>
988 Baker, John, Tim Griffis (2003-2010) AmeriFlux US-Ro3 Rosemount- G19, Dataset.
989 <https://doi.org/10.17190/AMF/1246093>
990 Baker, John, Tim Griffis (2003-2017) AmeriFlux US-Ro2 Rosemount- C7, Dataset.
991 <https://doi.org/10.17190/AMF/1418683>
992 Baker, John, Tim Griffis (2014-) AmeriFlux US-Ro4 Rosemount Prairie, Dataset.
993 <https://doi.org/10.17190/AMF/1419507>
994 Baker, John, Tim Griffis, Timothy Griffis (2003-2017) AmeriFlux US-Ro1 Rosemount- G21, Dataset.
995 <https://doi.org/10.17190/AMF/1246092>

- 996 Bernacchi, Carl (2004-2008) AmeriFlux US-Bo2 Bondville (companion site), Dataset.
 997 <https://doi.org/10.17190/AMF/1246037>
 998 Biraud, Sebastien, Marc Fischer, Stephen Chan, Margaret Torn (2002-) AmeriFlux US-ARM ARM Southern Great
 999 Plains site- Lamont, Dataset. <https://doi.org/10.17190/AMF/1246027>
 1000 Bohrer, Gil (2011-2016) AmeriFlux US-ORv Olentangy River Wetland Research Park, Dataset.
 1001 <https://doi.org/10.17190/AMF/1246135>
 1002 Bohrer, Gil, Janice Kerns (2015-2016) AmeriFlux US-OWC Old Woman Creek, Dataset.
 1003 <https://doi.org/10.17190/AMF/1418679>
 1004 Chen, Jiquan (2002-2002) AmeriFlux US-Wi8 Young hardwood clearcut (YHW), Dataset.
 1005 <https://doi.org/10.17190/AMF/1246023>
 1006 Chen, Jiquan (2002-2005) AmeriFlux US-Wi4 Mature red pine (MRP), Dataset.
 1007 <https://doi.org/10.17190/AMF/1246019>
 1008 Chen, Jiquan (2003-2003) AmeriFlux US-Wi1 Intermediate hardwood (IHW), Dataset.
 1009 <https://doi.org/10.17190/AMF/1246015>
 1010 Chen, Jiquan (2004-2004) AmeriFlux US-Wi5 Mixed young jack pine (MYJP), Dataset.
 1011 <https://doi.org/10.17190/AMF/1246020>
 1012 Chen, Jiquan (2004-2005) AmeriFlux US-Wi9 Young Jack pine (YJP), Dataset.
 1013 <https://doi.org/10.17190/AMF/1246024>
 1014 Chen, Jiquan (2005-2005) AmeriFlux US-Wi7 Red pine clearcut (RPCC), Dataset.
 1015 <https://doi.org/10.17190/AMF/1246022>
 1016 Chen, Jiquan, Housen Chu (2011-2013) AmeriFlux US-CRT Curtice Walter-Berger cropland, Dataset.
 1017 <https://doi.org/10.17190/AMF/1246156>
 1018 Chen, Jiquan, Housen Chu (2011-2013) AmeriFlux US-WPT Winous Point North Marsh, Dataset.
 1019 <https://doi.org/10.17190/AMF/1246155>
 1020 Chen, Jiquan, Housen Chu, Asko Noormets (2004-2013) AmeriFlux US-Oho Oak Openings, Dataset.
 1021 <https://doi.org/10.17190/AMF/1246089>
 1022 Clark, Ken (2004-) AmeriFlux US-Slt Silas Little- New Jersey, Dataset. <https://doi.org/10.17190/AMF/1246096>
 1023 Clark, Ken (2005-2008) AmeriFlux US-Dix Fort Dix, Dataset. <https://doi.org/10.17190/AMF/1246045>
 1024 Clark, Ken (2005-) AmeriFlux US-Ced Cedar Bridge, Dataset. <https://doi.org/10.17190/AMF/1246043>
 1025 Desai, Ankur (1996-) AmeriFlux US-PFa Park Falls/WLEF, Dataset. <https://doi.org/10.17190/AMF/1246090>
 1026 Desai, Ankur (1999-) AmeriFlux US-WCr Willow Creek, Dataset. <https://doi.org/10.17190/AMF/1246111>
 1027 Desai, Ankur (2001-) AmeriFlux US-Los Lost Creek, Dataset. <https://doi.org/10.17190/AMF/1246071>
 1028 Desai, Ankur (2001-) AmeriFlux US-Syv Sylvania Wilderness Area, Dataset. <https://doi.org/10.17190/AMF/1246106>
 1029 Drake, Bert, Ross Hinkle (2000-2007) AmeriFlux US-KS2 Kennedy Space Center (scrub oak), Dataset.
 1030 <https://doi.org/10.17190/AMF/1246070>
 1031 Gough, Christopher, Gil Bohrer, Peter Curtis (1999-) AmeriFlux US-UMB Univ. of Mich. Biological Station, Dataset.
 1032 <https://doi.org/10.17190/AMF/1246107>
 1033 Gough, Christopher, Gil Bohrer, Peter Curtis (2007-) AmeriFlux US-UMd UMBS Disturbance, Dataset.
 1034 <https://doi.org/10.17190/AMF/1246134>
 1035 Hadley, Julian, J. William Munger (2004-) AmeriFlux US-Ha2 Harvard Forest Hemlock Site, Dataset.
 1036 <https://doi.org/10.17190/AMF/1246060>
 1037 Heilman, Jim (2004-) AmeriFlux US-FR3 Freeman Ranch- Woodland, Dataset.
 1038 <https://doi.org/10.17190/AMF/1246055>
 1039 Hollinger, David (1996-) AmeriFlux US-Ho1 Howland Forest (main tower), Dataset.
 1040 <https://doi.org/10.17190/AMF/1246061>
 1041 Hollinger, David (1999-) AmeriFlux US-Ho2 Howland Forest (west tower), Dataset.
 1042 <https://doi.org/10.17190/AMF/1246062>
 1043 Hollinger, David (2000-) AmeriFlux US-Ho3 Howland Forest (harvest site), Dataset.
 1044 <https://doi.org/10.17190/AMF/1246063>
 1045 Lee, Xuhui (1999-2004) AmeriFlux US-GMF Great Mountain Forest, Dataset.
 1046 <https://doi.org/10.17190/AMF/1246057>
 1047 Matamala, Roser (2004-) AmeriFlux US-IB2 Fermi National Accelerator Laboratory- Batavia (Prairie site), Dataset.
 1048 <https://doi.org/10.17190/AMF/1246066>

- 1049 Matamala, Roser (2005-) AmeriFlux US-IB1 Fermi National Accelerator Laboratory- Batavia (Agricultural site),
1050 Dataset. <https://doi.org/10.17190/AMF/1246065>
- 1051 McCaughey, Harry (2003-) AmeriFlux CA-Gro Ontario - Groundhog River, Boreal Mixedwood Forest, Dataset.
<https://doi.org/10.17190/AMF/1245996>
- 1052 McFadden, Joe (2005-2009) AmeriFlux US-KUT KUOM Turfgrass Field, Dataset.
<https://doi.org/10.17190/AMF/1246145>
- 1053 Meyers, Tilden (1995-1999) AmeriFlux US-WBW Walker Branch Watershed, Dataset.
<https://doi.org/10.17190/AMF/1246109>
- 1054 Meyers, Tilden (1996-) AmeriFlux US-Bo1 Bondville, Dataset. <https://doi.org/10.17190/AMF/1246036>
- 1055 Meyers, Tilden (2002-2006) AmeriFlux US-Goo Goodwin Creek, Dataset. <https://doi.org/10.17190/AMF/1246058>
- 1056 Meyers, Tilden (2004-) AmeriFlux US-CaV Canaan Valley, Dataset. <https://doi.org/10.17190/AMF/1246042>
- 1057 Meyers, Tilden (2005-) AmeriFlux US-ChR Chestnut Ridge, Dataset. <https://doi.org/10.17190/AMF/1246044>
- 1058 Munger, J. William (1991-) AmeriFlux US-Ha1 Harvard Forest EMS Tower (HFR1), Dataset.
<https://doi.org/10.17190/AMF/1246059>
- 1059 Noormets, Asko (2005-) AmeriFlux US-NC2 NC_Loblolly Plantation, Dataset.
<https://doi.org/10.17190/AMF/1246083>
- 1060 Noormets, Asko (2005-2013) AmeriFlux US-NC1 NC_Clearcut, Dataset. <https://doi.org/10.17190/AMF/1246082>
- 1061 Noormets, Asko (2013-) AmeriFlux US-NC3 NC_Clearcut#3, Dataset. <https://doi.org/10.17190/AMF/1419506>
- 1062 Novick, Kim, Rich Phillips (1999-) AmeriFlux US-MMS Morgan Monroe State Forest, Dataset.
<https://doi.org/10.17190/AMF/1246080>
- 1063 Oishi, Chris, Kim Novick, Paul Stoy (2001-2008) AmeriFlux US-Dk1 Duke Forest-open field, Dataset.
<https://doi.org/10.17190/AMF/1246046>
- 1064 Oishi, Chris, Kim Novick, Paul Stoy (2001-2008) AmeriFlux US-Dk2 Duke Forest-hardwoods, Dataset.
<https://doi.org/10.17190/AMF/1246047>
- 1065 Oishi, Chris, Kim Novick, Paul Stoy (2001-2008) AmeriFlux US-Dk3 Duke Forest - loblolly pine, Dataset.
<https://doi.org/10.17190/AMF/1246048>
- 1066 Prueger, John, Tim Parkin (2001-) AmeriFlux US-Br1 Brooks Field Site 10- Ames, Dataset.
<https://doi.org/10.17190/AMF/1246038>
- 1067 Prueger, John, Tim Parkin (2001-) AmeriFlux US-Br3 Brooks Field Site 11- Ames, Dataset.
<https://doi.org/10.17190/AMF/1246039>
- 1068 Richardson, Andrew, David Hollinger (2004-) AmeriFlux US-Bar Bartlett Experimental Forest, Dataset.
<https://doi.org/10.17190/AMF/1246030>
- 1069 Sturtevant, Cove, David Durden, Stefan Metzger (2016-) AmeriFlux US-xSC NEON Smithsonian Conservation Biology Institute (SCBI), Dataset. <https://doi.org/10.17190/AMF/1671900>
- 1070 Sturtevant, Cove, David Durden, Stefan Metzger (2016-) AmeriFlux US-xSE NEON Smithsonian Environmental Research Center (SERC), Dataset. <https://doi.org/10.17190/AMF/1617734>
- 1071 Sturtevant, Cove, David Durden, Stefan Metzger (2017-) AmeriFlux US-xDL NEON Dead Lake (DELA), Dataset.
<https://doi.org/10.17190/AMF/1579721>
- 1072 Sturtevant, Cove, David Durden, Stefan Metzger (2017-) AmeriFlux US-xGR NEON Great Smoky Mountains National Park, Twin Creeks (GRSM), Dataset. <https://doi.org/10.17190/AMF/1634885>
- 1073 Sturtevant, Cove, David Durden, Stefan Metzger (2017-) AmeriFlux US-xST NEON Steigerwaldt Land Services (STEI), Dataset. <https://doi.org/10.17190/AMF/1617737>
- 1074 Sturtevant, Cove, David Durden, Stefan Metzger (2017-) AmeriFlux US-xTA NEON Talladega National Forest (TALL), Dataset. <https://doi.org/10.17190/AMF/1671902>
- 1075 Sturtevant, Cove, David Durden, Stefan Metzger (2017-) AmeriFlux US-xTR NEON Treehaven (TREE), Dataset.
<https://doi.org/10.17190/AMF/1634886>
- 1076 Sturtevant, Cove, David Durden, Stefan Metzger (2017-) AmeriFlux US-xUK NEON The University of Kansas Field Station (UKFS), Dataset. <https://doi.org/10.17190/AMF/1617740>
- 1077 Sturtevant, Cove, David Durden, Stefan Metzger (2017-) AmeriFlux US-xUN NEON University of Notre Dame Environmental Research Center (UNDE), Dataset. <https://doi.org/10.17190/AMF/1617741>
- 1078 Suyker, Andy (2001-) AmeriFlux US-Ne2 Mead - irrigated maize-soybean rotation site, Dataset.
<https://doi.org/10.17190/AMF/1246085>

- 1101 Suyker, Andy (2001-) AmeriFlux US-Ne3 Mead - rainfed maize-soybean rotation site, Dataset.
1102 https://doi.org/10.17190/AMF/1246086
1103 Torn, Margaret (2005-2006) AmeriFlux US-ARc ARM Southern Great Plains control site- Lamont, Dataset.
1104 https://doi.org/10.17190/AMF/1246026
1105 Wood, Jeffrey, Lianhong Gu (2004-) AmeriFlux US-MOz Missouri Ozark Site, Dataset.
1106 https://doi.org/10.17190/AMF/1246081
1107
1108

1109 **References**

- 1110 A. E. Schuh, Otte, M. J., Walko, R., Oda, T., & Ott, L. (2019). Using the Refined-Mesh Ocean-Land-
1111 Atmosphere-Model (OLAM) to Quantify Expected Carbon Dioxide Variations Across Urban
1112 Landscapes. Presented at the American Meteorological Society, Phoenix, AZ.
- 1113 Amthor, J. S. (2000). The McCree-de Wit-Penning de Vries-Thornley Respiration Paradigms: 30 Years
1114 Later. *Annals of Botany*, 86(1), 1–20. <https://doi.org/10.1006/anbo.2000.1175>
- 1115 Asefi-Najafabady, S., Rayner, P. J., Gurney, K. R., McRobert, A., Song, Y., Coltin, K., et al. (2014). A
1116 multiyear, global gridded fossil fuel CO₂ emission data product: Evaluation and analysis of
1117 results. *Journal of Geophysical Research: Atmospheres*, 119(17), 10,213-10,231.
1118 <https://doi.org/10.1002/2013JD021296>
- 1119 Aubinet, M. (2008). Eddy Covariance CO₂ Flux Measurements in Nocturnal Conditions: An Analysis of the
1120 Problem. *Ecological Applications*, 18(6), 1368–1378. <https://doi.org/10.1890/06-1336.1>
- 1121 Barr, A. G., Richardson, A. D., Hollinger, D. Y., Papale, D., Arain, M. A., Black, T. A., et al. (2013). Use of
1122 change-point detection for friction–velocity threshold evaluation in eddy-covariance studies.
1123 *Agricultural and Forest Meteorology*, 171–172, 31–45.
1124 <https://doi.org/10.1016/j.agrformet.2012.11.023>
- 1125 Basu, S., Lehman, S. J., Miller, J. B., Andrews, A. E., Sweeney, C., Gurney, K. R., et al. (2020). Estimating
1126 US fossil fuel CO₂ emissions from measurements of ¹⁴C in atmospheric CO₂. *Proceedings of the*
1127 *National Academy of Sciences*, 117(24), 13300–13307.
1128 <https://doi.org/10.1073/pnas.1919032117>
- 1129 Benjamin, S. G., Weygandt, S. S., Brown, J. M., Hu, M., Alexander, C. R., Smirnova, T. G., et al. (2016). A
1130 North American Hourly Assimilation and Model Forecast Cycle: The Rapid Refresh. *Monthly*
1131 *Weather Review*, 144(4), 1669–1694. <https://doi.org/10.1175/MWR-D-15-0242.1>
- 1132 Berry, J., Wolf, A., Campbell, J. E., Baker, I., Blake, N., Blake, D., et al. (2013). A coupled model of the
1133 global cycles of carbonyl sulfide and CO₂: A possible new window on the carbon cycle. *Journal of*
1134 *Geophysical Research: Biogeosciences*, 118(2), 842–852. <https://doi.org/10.1002/jgrg.20068>
- 1135 Buyantuyev, A., & Wu, J. (2009). Urbanization alters spatiotemporal patterns of ecosystem primary
1136 production: A case study of the Phoenix metropolitan region, USA. *Journal of Arid Environments*,
1137 73(4), 512–520. <https://doi.org/10.1016/j.jaridenv.2008.12.015>
- 1138 Chandrasekar, K., Sai, M. V. R. S., Roy, P. S., & Dwevedi, R. S. (2010). Land Surface Water Index (LSWI)
1139 response to rainfall and NDVI using the MODIS Vegetation Index product. *International Journal*
1140 *of Remote Sensing*, 31(15), 3987–4005. <https://doi.org/10.1080/01431160802575653>
- 1141 Corbin, K. D., Denning, A. S., Lokupitiya, E. Y., Schuh, A. E., Miles, N. L., Davis, K. J., et al. (2010). Assessing
1142 the impact of crops on regional CO₂ fluxes and atmospheric concentrations. *Tellus B: Chemical*
1143 *and Physical Meteorology*, 62(5), 521–532. <https://doi.org/10.1111/j.1600-0889.2010.00485.x>
- 1144 Elder, J. (2018). Chapter 16 - The Apparent Paradox of Complexity in Ensemble Modeling*. In R. Nisbet,
1145 G. Miner, & K. Yale (Eds.), *Handbook of Statistical Analysis and Data Mining Applications (Second*
1146 *Edition)* (pp. 705–718). Boston: Academic Press. <https://doi.org/10.1016/B978-0-12-416632-5.00016-5>
- 1147 Falge, E., Baldocchi, D., Tenhunen, J., Aubinet, M., Bakwin, P., Berbigier, P., et al. (2002). Seasonality of
1148 ecosystem respiration and gross primary production as derived from FLUXNET measurements.
1149 *Agricultural and Forest Meteorology*, 113(1), 53–74. [https://doi.org/10.1016/S0168-1923\(02\)00102-8](https://doi.org/10.1016/S0168-1923(02)00102-8)
- 1150 Farquhar, G. D., von Caemmerer, S., & Berry, J. A. (1980). A biochemical model of photosynthetic CO₂
1151 assimilation in leaves of C₃ species. *Planta*, 149(1), 78–90. <https://doi.org/10.1007/BF00386231>
- 1152 Feng, S., Lauvaux, T., Keller, K., Davis, K. J., Rayner, P., Oda, T., & Gurney, K. R. (2019). A Road Map for
1153 Improving the Treatment of Uncertainties in High-Resolution Regional Carbon Flux Inverse

- 1156 Estimates. *Geophysical Research Letters*, 46(22), 13461–13469.
1157 <https://doi.org/10.1029/2019GL082987>
- 1158 Feng, S., Lauvaux, T., Davis, K. J., Keller, K., Zhou, Y., Williams, C., et al. (2019). Seasonal Characteristics of
1159 Model Uncertainties From Biogenic Fluxes, Transport, and Large-Scale Boundary Inflow in
1160 Atmospheric CO₂ Simulations Over North America. *Journal of Geophysical Research: Atmospheres*, 124(24), 14325–14346. <https://doi.org/10.1029/2019JD031165>
- 1161 Fisher, J. B., Sikka, M., Huntzinger, D. N., Schwalm, C., & Liu, J. (2016). Technical note: 3-hourly temporal
1162 downscaling of monthly global terrestrial biosphere model net ecosystem exchange.
1163 *Biogeosciences*, 13(14), 4271–4277. <https://doi.org/10.5194/bg-13-4271-2016>
- 1164 Flexas, J., Bota, J., Galmés, J., Medrano, H., & Ribas-Carbó, M. (2006). Keeping a positive carbon balance
1165 under adverse conditions: responses of photosynthesis and respiration to water stress.
1166 *Physiologia Plantarum*, 127(3), 343–352. <https://doi.org/10.1111/j.1399-3054.2006.00621.x>
- 1167 Golubiewski, N. E. (2006). Urbanization Increases Grassland Carbon Pools: Effects Of Landscaping In
1168 Colorado's Front Range. *Ecological Applications*, 16(2), 555–571. [https://doi.org/10.1890/1051-0761\(2006\)016\[0555:UIGCPE\]2.0.CO;2](https://doi.org/10.1890/1051-0761(2006)016[0555:UIGCPE]2.0.CO;2)
- 1169 Gourdji, S. M., Hirsch, A. I., Mueller, K. L., Yadav, V., Andrews, A. E., & Michalak, A. M. (2010). Regional-
1170 scale geostatistical inverse modeling of North American CO₂ fluxes: a synthetic data study.
1171 *Atmospheric Chemistry and Physics*, 10(13), 6151–6167. <https://doi.org/10.5194/acp-10-6151-2010>
- 1172 Gourdji, S. M., Mueller, K. L., Yadav, V., Huntzinger, D. N., Andrews, A. E., Trudeau, M., et al. (2012).
1173 North American CO₂ exchange: inter-comparison of modeled estimates with results from a fine-
1174 scale atmospheric inversion. *Biogeosciences*, 9(1), 457–475. <https://doi.org/10.5194/bg-9-457-2012>
- 1175 Gray, J. M., Frolking, S., Kort, E. A., Ray, D. K., Kucharik, C. J., Ramankutty, N., & Friedl, M. A. (2014).
1176 Direct human influence on atmospheric CO₂ seasonality from increased cropland productivity.
1177 *Nature*, 515(7527), 398–401. <https://doi.org/10.1038/nature13957>
- 1178 Guindin-Garcia, N., Gitelson, A. A., Arkebauer, T. J., Shanahan, J., & Weiss, A. (2012). An evaluation of
1179 MODIS 8- and 16-day composite products for monitoring maize green leaf area index.
1180 *Agricultural and Forest Meteorology*, 161, 15–25.
1181 <https://doi.org/10.1016/j.agrformet.2012.03.012>
- 1182 Gurney, Kevin R., Liang, J., Patarasuk, R., Song, Y., Huang, J., & Roest, G. (2020). The Vulcan Version 3.0
1183 High-Resolution Fossil Fuel CO₂ Emissions for the United States. *Journal of Geophysical
1184 Research: Atmospheres*, 125(19), e2020JD032974. <https://doi.org/10.1029/2020JD032974>
- 1185 Gurney, Kevin Robert, Law, R. M., Denning, A. S., Rayner, P. J., Baker, D., Bousquet, P., et al. (2002).
1186 Towards robust regional estimates of CO₂ sources and sinks using atmospheric transport
1187 models. *Nature*, 415(6872), 626–630. <https://doi.org/10.1038/415626a>
- 1188 Hardiman, B. S., Wang, J. A., Hutyra, L. R., Gately, C. K., Getson, J. M., & Friedl, M. A. (2017). Accounting
1189 for urban biogenic fluxes in regional carbon budgets. *The Science of the Total Environment*, 592,
1190 366–372. <https://doi.org/10.1016/j.scitotenv.2017.03.028>
- 1191 Haynes, K. D., Baker, I. T., Denning, A. S., Stöckli, R., Schaefer, K., Lokupitiya, E. Y., & Haynes, J. M. (2019).
1192 Representing Grasslands Using Dynamic Prognostic Phenology Based on Biological Growth
1193 Stages: 1. Implementation in the Simple Biosphere Model (SiB4). *Journal of Advances in
1194 Modeling Earth Systems*, 11(12), 4423–4439. <https://doi.org/10.1029/2018MS001540>
- 1195 Haynes, Katherine D., Baker, I. T., Denning, A. S., Wolf, S., Wohlfahrt, G., Kiely, G., et al. (2019).
1196 Representing Grasslands Using Dynamic Prognostic Phenology Based on Biological Growth
1197 Stages: Part 2. Carbon Cycling. *Journal of Advances in Modeling Earth Systems*, 11(12), 4440–
1198 4465. <https://doi.org/10.1029/2018MS001541>

- 1203 Hilton, T. W., Davis, K. J., Keller, K., & Urban, N. M. (2013). Improving North American terrestrial CO₂ flux
1204 diagnosis using spatial structure in land surface model residuals. *Biogeosciences*, 10(7), 4607–
1205 4625. <https://doi.org/10.5194/bg-10-4607-2013>
- 1206 Hilton, T. W., Davis, K. J., & Keller, K. (2014). Evaluating terrestrial CO₂ flux diagnoses and uncertainties
1207 from a simple land surface model and its residuals. *Biogeosciences*, 11(2), 217–235.
1208 <https://doi.org/10.5194/bg-11-217-2014>
- 1209 Hilton, Timothy W., Whelan, M. E., Zumkehr, A., Kulkarni, S., Berry, J. A., Baker, I. T., et al. (2017). Peak
1210 growing season gross uptake of carbon in North America is largest in the Midwest USA. *Nature*
1211 *Climate Change*, 7(6), 450–454. <https://doi.org/10.1038/nclimate3272>
- 1212 Högberg, P., Nordgren, A., Buchmann, N., Taylor, A. F., Ekblad, A., Högberg, M. N., et al. (2001). Large-
1213 scale forest girdling shows that current photosynthesis drives soil respiration. *Nature*,
1214 411(6839), 789–792. <https://doi.org/10.1038/35081058>
- 1215 Hu, L., Andrews, A. E., Thoning, K. W., Sweeney, C., Miller, J. B., Michalak, A. M., et al. (2019). Enhanced
1216 North American carbon uptake associated with El Niño. *Science Advances*, 5(6), eaaw0076.
1217 <https://doi.org/10.1126/sciadv.aaw0076>
- 1218 Hu, X.-M., Gourdji, S., Davis, K. J., Wang, Q., Zhang, Y., Xue, M., et al. (in review). Implementation of
1219 improved parameterization of terrestrial flux in WRF-VPRM improves the simulation of
1220 nighttime CO₂ peaks and a daytime CO₂ band ahead of a cold front. *Journal of Geophysical*
1221 *Research: Atmospheres*.
- 1222 Jacobson, A. R., Schuldt, K. N., Miller, J. B., Oda, T., Tans, P., Andrews, A., et al. (2020). CarbonTracker
1223 CT2019B. <https://doi.org/10.25925/20201008>
- 1224 Jassal, R. S., Black, T. A., Cai, T., Morgenstern, K., Li, Z., Gaumont-Guay, D., & Nesic, Z. (2007).
1225 Components of ecosystem respiration and an estimate of net primary productivity of an
1226 intermediate-aged Douglas-fir stand. *Agricultural and Forest Meteorology*, 144(1), 44–57.
1227 <https://doi.org/10.1016/j.agrformet.2007.01.011>
- 1228 Jin, S., Homer, C., Yang, L., Danielson, P., Dewitz, J., Li, C., et al. (2019). Overall Methodology Design for
1229 the United States National Land Cover Database 2016 Products. *Remote Sensing*, 11(24), 2971.
1230 <https://doi.org/10.3390/rs11242971>
- 1231 Joiner, J., Yoshida, Y., Vasilkov, A. P., Yoshida, Y., Corp, L. A., & Middleton, E. M. (2011). First
1232 observations of global and seasonal terrestrial chlorophyll fluorescence from space.
1233 *Biogeosciences*, 8(3), 637–651. <https://doi.org/10.5194/bg-8-637-2011>
- 1234 Karion, A., Callahan, W., Stock, M., Prinzivalli, S., Verhulst, K. R., Kim, J., et al. (2020). Greenhouse gas
1235 observations from the Northeast Corridor tower network. *Earth System Science Data*, 12(1),
1236 699–717. <https://doi.org/10.5194/essd-12-699-2020>
- 1237 Karion, A., Lopez-Coto, I., Gourdji, S. M., Mueller, K., Ghosh, S., Callahan, W., et al. (2021). Background
1238 conditions for an urban greenhouse gas network in the Washington, D.C. and Baltimore
1239 metropolitan region. *Atmospheric Chemistry and Physics Discussions*, 1–27.
1240 <https://doi.org/10.5194/acp-2020-1256>
- 1241 Lasslop, G., Reichstein, M., Papale, D., Richardson, A. D., Arneth, A., Barr, A., et al. (2010). Separation of
1242 net ecosystem exchange into assimilation and respiration using a light response curve approach:
1243 critical issues and global evaluation. *Global Change Biology*, 16(1), 187–208.
1244 <https://doi.org/10.1111/j.1365-2486.2009.02041.x>
- 1245 Lauvaux, T., Uliasz, M., Sarrat, C., Chevallier, F., Bousquet, P., Lac, C., et al. (2008). Mesoscale inversion:
1246 first results from the CERES campaign with synthetic data. *Atmospheric Chemistry and Physics*,
1247 8(13), 3459–3471. <https://doi.org/10.5194/acp-8-3459-2008>
- 1248 Lauvaux, T., Schuh, A. E., Uliasz, M., Richardson, S., Miles, N., Andrews, A. E., et al. (2012). Constraining
1249 the CO₂ budget of the corn belt: exploring uncertainties from the assumptions in a mesoscale

- 1250 inverse system. *Atmospheric Chemistry and Physics*, 12(1), 337–354.
1251 <https://doi.org/10.5194/acp-12-337-2012>
- 1252 Lauvaux, Thomas, Gurney, K. R., Miles, N. L., Davis, K. J., Richardson, S. J., Deng, A., et al. (2021). Policy-
1253 Relevant Assessment of Urban CO₂ Emissions | Environmental Science & Technology. Retrieved
1254 from <https://pubs.acs.org/doi/abs/10.1021/acs.est.0c00343>
- 1255 Li, X., Hu, X.-M., Cai, C., Jia, Q., Zhang, Y., Liu, J., et al. (2020). Terrestrial CO₂ Fluxes, Concentrations,
1256 Sources and Budget in Northeast China: Observational and Modeling Studies. *Journal of*
1257 *Geophysical Research: Atmospheres*, 125(6), e2019JD031686.
1258 <https://doi.org/10.1029/2019JD031686>
- 1259 Lin, J. C., Gerbig, C., Wofsy, S. C., Andrews, A. E., Daube, B. C., Davis, K. J., & Grainger, C. A. (2003). A
1260 near-field tool for simulating the upstream influence of atmospheric observations: The
1261 Stochastic Time-Inverted Lagrangian Transport (STILT) model. *Journal of Geophysical Research: Atmospheres*, 108(D16). <https://doi.org/10.1029/2002JD003161>
- 1262 Lokupitiya, E., Denning, S., Paustian, K., Baker, I., Schaefer, K., Verma, S., et al. (2009). Incorporation of
1263 crop phenology in Simple Biosphere Model (SiBcrop) to improve land-atmosphere carbon
1264 exchanges from croplands. *Biogeosciences*, 6(6), 969–986. <https://doi.org/10.5194/bg-6-969-2009>
- 1265 Lopez-Coto, I., Ghosh, S., Prasad, K., & Whetstone, J. (2017). Tower-based greenhouse gas measurement
1266 network design—The National Institute of Standards and Technology North East Corridor
1267 Testbed. *Advances in Atmospheric Sciences*, 34(9), 1095–1105. <https://doi.org/10.1007/s00376-017-6094-6>
- 1268 Luus, K. A., & Lin, J. C. (2015). The Polar Vegetation Photosynthesis and Respiration Model: a
1269 parsimonious, satellite-data-driven model of high-latitude CO₂ exchange. *Geoscientific Model
1270 Development*, 8(8), 2655–2674. <https://doi.org/10.5194/gmd-8-2655-2015>
- 1271 Mahadevan, P., Wofsy, S. C., Matross, D. M., Xiao, X., Dunn, A. L., Lin, J. C., et al. (2008). A satellite-based
1272 biosphere parameterization for net ecosystem CO₂ exchange: Vegetation Photosynthesis and
1273 Respiration Model (VPRM). *Global Biogeochemical Cycles*, 22(2).
1274 <https://doi.org/10.1029/2006GB002735>
- 1275 Martin, C. R., Zeng, N., Karion, A., Mueller, K., Ghosh, S., Lopez-Coto, I., et al. (2019). Investigating
1276 sources of variability and error in simulations of carbon dioxide in an urban region. *Atmospheric
1277 Environment*, 199, 55–69. <https://doi.org/10.1016/j.atmosenv.2018.11.013>
- 1278 Meir, P., Metcalfe, D. b, Costa, A. c. l, & Fisher, R. a. (2008). The fate of assimilated carbon during
1279 drought: impacts on respiration in Amazon rainforests. *Philosophical Transactions of the Royal
1280 Society B: Biological Sciences*, 363(1498), 1849–1855. <https://doi.org/10.1098/rstb.2007.0021>
- 1281 Miles, N. L., Richardson, S. J., Martins, D. K., Davis, K. J., Lauvaux, T., Haupt, B. J., & Miller, S. K. (2018).
1282 ACT-America: L2 In Situ CO₂, CO, and CH₄ Concentrations from Towers, Eastern USA. ORNL
1283 DAAC. <https://doi.org/10.3334/ORNLDAAAC/1568>
- 1284 Miller, J. B., Lehman, S. J., Verhulst, K. R., Miller, C. E., Duren, R. M., Yadav, V., et al. (2020). Large and
1285 seasonally varying biospheric CO₂ fluxes in the Los Angeles megacity revealed by atmospheric
1286 radiocarbon. *Proceedings of the National Academy of Sciences*, 117(43), 26681–26687.
1287 <https://doi.org/10.1073/pnas.2005253117>
- 1288 Mitchell, L., Lin, J. C., Hutyra, L. R., Sargent, M., Wofsy, S. C., Miles, N. L., et al. (2019). NACP: Urban
1289 Greenhouse Gases across the CO₂ Urban Synthesis and Analysis Network. ORNL DAAC.
1290 <https://doi.org/10.3334/ORNLDAAAC/1743>
- 1291 Molchanov, A. G. (2009). Effect of moisture availability on photosynthetic productivity and autotrophic
1292 respiration of an oak stand. *Russian Journal of Plant Physiology*, 56(6), 769.
1293 <https://doi.org/10.1134/S1021443709060065>

- 1297 Moriasi, D. N., Arnold, J. G., Van Liew, M. W., Bingner, R. L., Harmel, R. D., & Veith, T. L. (2007). Model
1298 Evaluation Guidelines for Systematic Quantification of Accuracy in Watershed Simulations.
1299 *Transactions of the ASABE*, 50(3), 885–900.
- 1300 Mueller, K., Yadav, V., Lopez-Coto, I., Karion, A., Gourdji, S., Martin, C., & Whetstone, J. (2018). Siting
1301 Background Towers to Characterize Incoming Air for Urban Greenhouse Gas Estimation: A Case
1302 Study in the Washington, DC/Baltimore Area. *Journal of Geophysical Research: Atmospheres*,
1303 123(5), 2910–2926. <https://doi.org/10.1002/2017JD027364>
- 1304 NCEI, NWS, NOAA, & US DOC. (2020). North American Mesoscale Forecast System (NAM) [12 km].
1305 Retrieved February 7, 2021, from <https://www.ncei.noaa.gov/access/metadata/landing-page/bin/iso?id=gov.noaa.ncdc:C00630>
- 1306 Nicolini, G., Aubinet, M., Feigenwinter, C., Heinesch, B., Lindroth, A., Mamadou, O., et al. (2018). Impact
1307 of CO₂ storage flux sampling uncertainty on net ecosystem exchange measured by eddy
1308 covariance. *Agricultural and Forest Meteorology*, 248, 228–239.
1309 <https://doi.org/10.1016/j.agrformet.2017.09.025>
- 1310 NOAA Earth System Research Laboratory, Global Monitoring Division. (2019). Cooperative Global
1311 Atmospheric Data Integration Project (2019): Multi-laboratory compilation of atmospheric
1312 carbon dioxide data for the period 1957-2018;
1313 obspack_co2_1_GLOBALVIEWplus_v5.0_2019_08_12. Retrieved from
1314 <http://dx.doi.org/10.25925/20190812>
- 1315 Nowak, D. J., & Crane, D. E. (2002). Carbon storage and sequestration by urban trees in the USA.
1316 *Environmental Pollution*, 116(3), 381–389. [https://doi.org/10.1016/S0269-7491\(01\)00214-7](https://doi.org/10.1016/S0269-7491(01)00214-7)
- 1317 Parazoo, N. C., Frankenberg, C., Köhler, P., Joiner, J., Yoshida, Y., Magney, T., et al. (2019). Towards a
1318 Harmonized Long-Term Spaceborne Record of Far-Red Solar-Induced Fluorescence. *Journal of
1319 Geophysical Research: Biogeosciences*, 124(8), 2518–2539.
1320 <https://doi.org/10.1029/2019JG005289>
- 1321 Parton, W. J., Stewart, J. W. B., & Cole, C. V. (1988). Dynamics of C, N, P and S in Grassland Soils: A
1322 Model. *Biogeochemistry*, 5(1), 109–131.
- 1323 Peters, W., Krol, M. C., Werf, G. R. V. D., Houweling, S., Jones, C. D., Hughes, J., et al. (2010). Seven years
1324 of recent European net terrestrial carbon dioxide exchange constrained by atmospheric
1325 observations. *Global Change Biology*, 16(4), 1317–1337. <https://doi.org/10.1111/j.1365-2486.2009.02078.x>
- 1326 Pillai, D., Gerbig, C., Ahmadov, R., Rödenbeck, C., Kretschmer, R., Koch, T., et al. (2011). High-resolution
1327 simulations of atmospheric CO₂ over complex terrain – representing the Ochsenkopf mountain
1328 tall tower. *Atmospheric Chemistry and Physics*, 11(15), 7445–7464. <https://doi.org/10.5194/acp-11-7445-2011>
- 1329 Pitt, J. R., Lopez-Coto, I., Hajny, K. D. D., Mendoza Tomlin, J., Kaeser, R., Jayarathne, T., et al. (2020). New
1330 York City greenhouse gas emissions estimated with inverse modeling of aircraft measurements.
1331 Presented at the AGU Fall Meeting 2020, AGU.
- 1332 Potter, C. S., Randerson, J. T., Field, C. B., Matson, P. A., Vitousek, P. M., Mooney, H. A., & Klooster, S. A.
1333 (1993). Terrestrial ecosystem production: A process model based on global satellite and surface
1334 data. *Global Biogeochemical Cycles*, 7(4), 811–841. <https://doi.org/10.1029/93GB02725>
- 1335 Raciti, S. M., Hutyra, L. R., & Newell, J. D. (2014). Mapping carbon storage in urban trees with multi-
1336 source remote sensing data: relationships between biomass, land use, and demographics in
1337 Boston neighborhoods. *The Science of the Total Environment*, 500–501, 72–83.
1338 <https://doi.org/10.1016/j.scitotenv.2014.08.070>
- 1339 Raczka, B. M., Davis, K. J., Huntzinger, D., Neilson, R. P., Poulter, B., Richardson, A. D., et al. (2013).
1340 Evaluation of continental carbon cycle simulations with North American flux tower observations.
1341 *Ecological Monographs*, 83(4), 531–556. <https://doi.org/10.1890/12-0893.1>

- 1345 Randerson, J. T., Thompson, M. V., Malmstrom, C. M., Field, C. B., & Fung, I. Y. (1996). Substrate
1346 limitations for heterotrophs: Implications for models that estimate the seasonal cycle of
1347 atmospheric CO₂. *Global Biogeochemical Cycles*, 10(4), 585–602.
1348 <https://doi.org/10.1029/96GB01981>
- 1349 Reichstein, M., Falge, E., Baldocchi, D., Papale, D., Aubinet, M., Berbigier, P., et al. (2005). On the
1350 separation of net ecosystem exchange into assimilation and ecosystem respiration: review and
1351 improved algorithm. *Global Change Biology*, 11(9), 1424–1439. <https://doi.org/10.1111/j.1365-2486.2005.001002.x>
- 1353 Richardson, A. D., Anderson, R. S., Arain, M. A., Barr, A. G., Bohrer, G., Chen, G., et al. (2012). Terrestrial
1354 biosphere models need better representation of vegetation phenology: results from the North
1355 American Carbon Program Site Synthesis. *Global Change Biology*, 18(2), 566–584.
1356 <https://doi.org/10.1111/j.1365-2486.2011.02562.x>
- 1357 Richardson, S. J., Miles, N. L., Davis, K. J., Lauvaux, T., Martins, D. K., Turnbull, J. C., et al. (2017). Tower
1358 measurement network of in-situ CO₂, CH₄, and CO in support of the Indianapolis FLUX (INFLUX)
1359 Experiment. *Elementa: Science of the Anthropocene*, 5(59).
1360 <https://doi.org/10.1525/elementa.140>
- 1361 Rödenbeck, C., Houweling, S., Gloor, M., & Heimann, M. (2003). CO₂ flux history 1982–2001 inferred
1362 from atmospheric data using a global inversion of atmospheric transport. *Atmospheric
1363 Chemistry and Physics*, 3(6), 1919–1964. <https://doi.org/10.5194/acp-3-1919-2003>
- 1364 Sargent, M., Barrera, Y., Nehrkorn, T., Hutyra, L. R., Gately, C. K., Jones, T., et al. (2018). Anthropogenic
1365 and biogenic CO₂ fluxes in the Boston urban region. *Proceedings of the National Academy of
1366 Sciences*, 115(29), 7491–7496. <https://doi.org/10.1073/pnas.1803715115>
- 1367 Schwalm, C. R., Williams, C. A., Schaefer, K., Anderson, R., Arain, M. A., Baker, I., et al. (2010). A model-
1368 data intercomparison of CO₂ exchange across North America: Results from the North American
1369 Carbon Program site synthesis. *Journal of Geophysical Research: Biogeosciences*, 115(G3).
1370 <https://doi.org/10.1029/2009JG001229>
- 1371 Sellers, P. J., Mintz, Y., Sud, Y. C., & Dalcher, A. (1986). A Simple Biosphere Model (SIB) for Use within
1372 General Circulation Models. *Journal of Atmospheric Sciences*, 43(6), 505–531.
1373 [https://doi.org/10.1175/1520-0469\(1986\)043<0505:ASBMFU>2.0.CO;2](https://doi.org/10.1175/1520-0469(1986)043<0505:ASBMFU>2.0.CO;2)
- 1374 Sellers, P. J., Randall, D. A., Collatz, G. J., Berry, J. A., Field, C. B., Dazlich, D. A., et al. (1996). A Revised
1375 Land Surface Parameterization (SiB2) for Atmospheric GCMS. Part I: Model Formulation. *Journal
1376 of Climate*, 9(4), 676–705. [https://doi.org/10.1175/1520-0442\(1996\)009<0676:ARLSPF>2.0.CO;2](https://doi.org/10.1175/1520-0442(1996)009<0676:ARLSPF>2.0.CO;2)
- 1377 Shiga, Y. P., Michalak, A. M., Gourdji, S. M., Mueller, K. L., & Yadav, V. (2014). Detecting fossil fuel
1378 emissions patterns from subcontinental regions using North American in situ CO₂
1379 measurements. *Geophysical Research Letters*, 41(12), 4381–4388.
1380 <https://doi.org/10.1002/2014GL059684>
- 1381 Shiga, Y. P., Tadić, J. M., Qiu, X., Yadav, V., Andrews, A. E., Berry, J. A., & Michalak, A. M. (2018).
1382 Atmospheric CO₂ Observations Reveal Strong Correlation Between Regional Net Biospheric
1383 Carbon Uptake and Solar-Induced Chlorophyll Fluorescence. *Geophysical Research Letters*, 45(2),
1384 1122–1132. <https://doi.org/10.1002/2017GL076630>
- 1385 Skamarock, W., Klemp, J., Dudhia, J., Gill, D., Barker, D., Wang, W., et al. (2008). *A Description of the
1386 Advanced Research WRF Version 3 [Application/pdf]* (p. 1002 KB). UCAR/NCAR.
1387 <https://doi.org/10.5065/D68S4MVH>
- 1388 Turner, A. J., & Jacob, D. J. (2015). Balancing aggregation and smoothing errors in inverse models.
1389 *Atmospheric Chemistry and Physics*, 15(12), 7039–7048. <https://doi.org/10.5194/acp-15-7039-2015>

- 1391 Turner, Alexander J., Köhler, P., Magney, T. S., Frankenberg, C., Fung, I., & Cohen, R. C. (2020). A double
1392 peak in the seasonality of California's photosynthesis as observed from space. *Biogeosciences*,
1393 17(2), 405–422. <https://doi.org/10.5194/bg-17-405-2020>
- 1394 Wang, X., Dannenberg, M. P., Yan, D., Jones, M. O., Kimball, J. S., Moore, D. J. P., et al. (2020). Globally
1395 Consistent Patterns of Asynchrony in Vegetation Phenology Derived From Optical, Microwave,
1396 and Fluorescence Satellite Data. *Journal of Geophysical Research: Biogeosciences*, 125(7),
1397 e2020JG005732. <https://doi.org/10.1029/2020JG005732>
- 1398 Wang, Y., Deutscher, N. M., Palm, M., Warneke, T., Notholt, J., Baker, I., et al. (2016). Towards
1399 understanding the variability in biospheric CO₂ fluxes: using FTIR spectrometry and a chemical
1400 transport model to investigate the sources and sinks of carbonyl sulfide and its link to CO₂.
1401 *Atmospheric Chemistry and Physics*, 16(4), 2123–2138. <https://doi.org/10.5194/acp-16-2123-2016>
- 1402 Xiao, J., Davis, K. J., Urban, N. M., Keller, K., & Saliendra, N. Z. (2011). Upscaling carbon fluxes from
1403 towers to the regional scale: Influence of parameter variability and land cover representation on
1404 regional flux estimates. *Journal of Geophysical Research: Biogeosciences*, 116(G3).
1405 <https://doi.org/10.1029/2010JG001568>
- 1406 Xiao, X., Hollinger, D., Aber, J., Goltz, M., Davidson, E. A., Zhang, Q., & Iii, B. M. (2004). Satellite-based
1407 modeling of gross primary production in an evergreen needleleaf forest. Retrieved from
1408 <https://www.nrs.fs.fed.us/pubs/6798>
- 1409 Yadav, V., Michalak, A. M., Ray, J., & Shiga, Y. P. (2016). A statistical approach for isolating fossil fuel
1410 emissions in atmospheric inverse problems. *Journal of Geophysical Research: Atmospheres*,
1411 121(20), 12,490–12,504. <https://doi.org/10.1002/2016JD025642>
- 1412 Yang, L., Jin, S., Danielson, P., Homer, C., Gass, L., Bender, S. M., et al. (2018). A new generation of the
1413 United States National Land Cover Database: Requirements, research priorities, design, and
1414 implementation strategies. *ISPRS Journal of Photogrammetry and Remote Sensing*, 146, 108–
1415 123. <https://doi.org/10.1016/j.isprsjprs.2018.09.006>
- 1416 Yi, C., Davis, K. J., Bakwin, P. S., Berger, B. W., & Marr, L. C. (2000). Influence of advection on
1417 measurements of the net ecosystem-atmosphere exchange of CO₂ from a very tall tower.
1418 *Journal of Geophysical Research: Atmospheres*, 105(D8), 9991–9999.
1419 <https://doi.org/10.1029/2000JD900080>
- 1420 Zeng, N., Zhao, F., Collatz, G. J., Kalnay, E., Salawitch, R. J., West, T. O., & Guanter, L. (2014). Agricultural
1421 Green Revolution as a driver of increasing atmospheric CO₂ seasonal amplitude. *Nature*,
1422 515(7527), 394–397. <https://doi.org/10.1038/nature13893>
- 1423 Zhou, Y., Williams, C. A., Lauvaux, T., Davis, K. J., Feng, S., Baker, I., et al. (2020). A Multiyear Gridded
1424 Data Ensemble of Surface Biogenic Carbon Fluxes for North America: Evaluation and Analysis of
1425 Results. *Journal of Geophysical Research: Biogeosciences*, 125(2), e2019JG005314.
1426 <https://doi.org/10.1029/2019JG005314>
- 1427 Zhou, Y., Williams, C.A., Lauvaux, T., Feng, S., Baker, I.T., Wei, Y., et al. (2020). Atmospheric Carbon and
1428 Transport - America (ACT-America)ACT-America: Gridded Ensembles of Surface Biogenic Carbon
1429 Fluxes, 2003-2019 (Version 1.1) [NetCDF], 0 MB. <https://doi.org/10.3334/ORNLDAC/1675>
- 1430
- 1431

Tables & Figures

Table 1: Comparison of features across the three versions of VPRM.

	VPRM_{ann}	VPRM_{seas}	VPRM_{new}
Respiration model	original model: linear function of temperature	original model: linear function of temperature	expanded model including EVI, non-linear temperature and interactions with water stress
Parameter seasonality	no	yes (winter, spring, summer, fall)	no
Optimization technique	GPP and R _e parameters optimized simultaneously	GPP and R _e parameters optimized simultaneously	R _e parameters optimized with night-time data; GPP parameters optimized separately after subtracting predicted R _e from daytime NEE observations

Table 2: median across towers of the absolute monthly mean bias of simulated – observed biologic CO₂ enhancements for each biospheric model and month, using both WRF-STILT, NAMS-STILT and the mean of WRF-STILT and NAMS-STILT convolutions. Model/month combinations with a median absolute error less than 1 μmol/mol are shaded in light yellow, from 1 μmol/mol to 1.5 μmol/mol in dark yellow and > 1.5 μmol/mol in peach. The model(s) with the smallest median absolute bias (within 0.1 umol/mol) for each month is (are) highlighted in bold. The last row shows the value across all towers in the full year (where the number of towers varies by month).

	WRF-STILT					NAMS-STILT					Mean WRF-STILT & NAMS-STILT				
	VPRM _{ann}	VPRM _{seas}	VPRM _{new}	CASA	SiB4	VPRM _{ann}	VPRM _{seas}	VPRM _{new}	CASA	SiB4	VPRM _{ann}	VPRM _{seas}	VPRM _{new}	CASA	SiB4
201611	0.54	0.46	0.68	1.03	1.02	0.72	0.68	1.03	0.54	0.85	0.59	0.64	0.89	0.88	0.85
201612	1.72	2.39	1.82	0.88	0.93	2.04	2.66	2.21	1.29	1.02	1.87	2.63	2.07	1.15	0.96
201701	1.20	1.75	1.43	1.03	1.33	1.29	2.01	1.50	1.15	1.84	1.24	1.78	1.49	0.99	1.66
201702	0.67	0.54	0.51	1.55	1.35	0.41	0.59	0.71	1.62	1.27	0.38	0.56	0.65	1.54	1.31
201703	0.46	0.58	0.43	0.53	0.83	0.32	0.56	0.35	0.65	0.89	0.42	0.50	0.33	0.59	0.87
201704	0.31	0.57	0.54	0.63	0.82	0.72	0.59	0.51	0.64	1.23	0.59	0.52	0.54	0.55	1.14
201705	0.65	0.60	0.41	1.67	1.00	0.76	0.76	0.44	1.46	1.00	0.63	0.74	0.37	1.63	0.89
201706	0.85	1.56	1.05	1.46	1.41	2.18	1.01	1.02	0.59	0.87	1.43	0.96	0.98	1.02	0.82
201707	2.03	1.01	1.10	1.05	1.77	3.34	2.37	1.07	1.08	3.08	2.59	1.75	0.99	0.76	2.35
201708	1.59	0.78	0.88	0.95	0.68	2.29	0.90	1.49	0.66	0.74	1.58	0.92	1.26	0.70	0.90
201709	0.82	1.07	1.87	0.87	2.15	0.67	1.29	1.95	0.72	2.32	0.86	1.22	1.95	0.84	2.25
201710	0.49	0.48	0.72	1.46	0.96	0.64	0.75	0.50	1.37	1.20	0.45	0.61	0.61	1.33	1.11
<i>Full year</i>	0.83	0.82	0.89	1.09	1.16	1.02	1.02	0.99	0.96	1.17	0.93	0.93	0.88	0.94	1.14

Figure 1: Map of dominant land cover in domain at 0.02° in eastern USA and Canada, with a rectangle around the flux simulation domain (left panel). Also shown are the flux towers included in the historical parameter optimization (triangles), with the towers used for model evaluation in 2016/ 2017 explicitly labeled. (Labeled towers with star symbols are included in the 2017 evaluation, but not the historical parameter optimization.) Deciduous broadleaf forest and cropland pixels used for spatial aggregation are shown in the panel on the right, with these pixels selected as containing $> 50\%$ coverage at 0.1° for VPRM and CASA, and $> 25\%$ for SiB4 at 0.5° (Table S1; Figure S6).

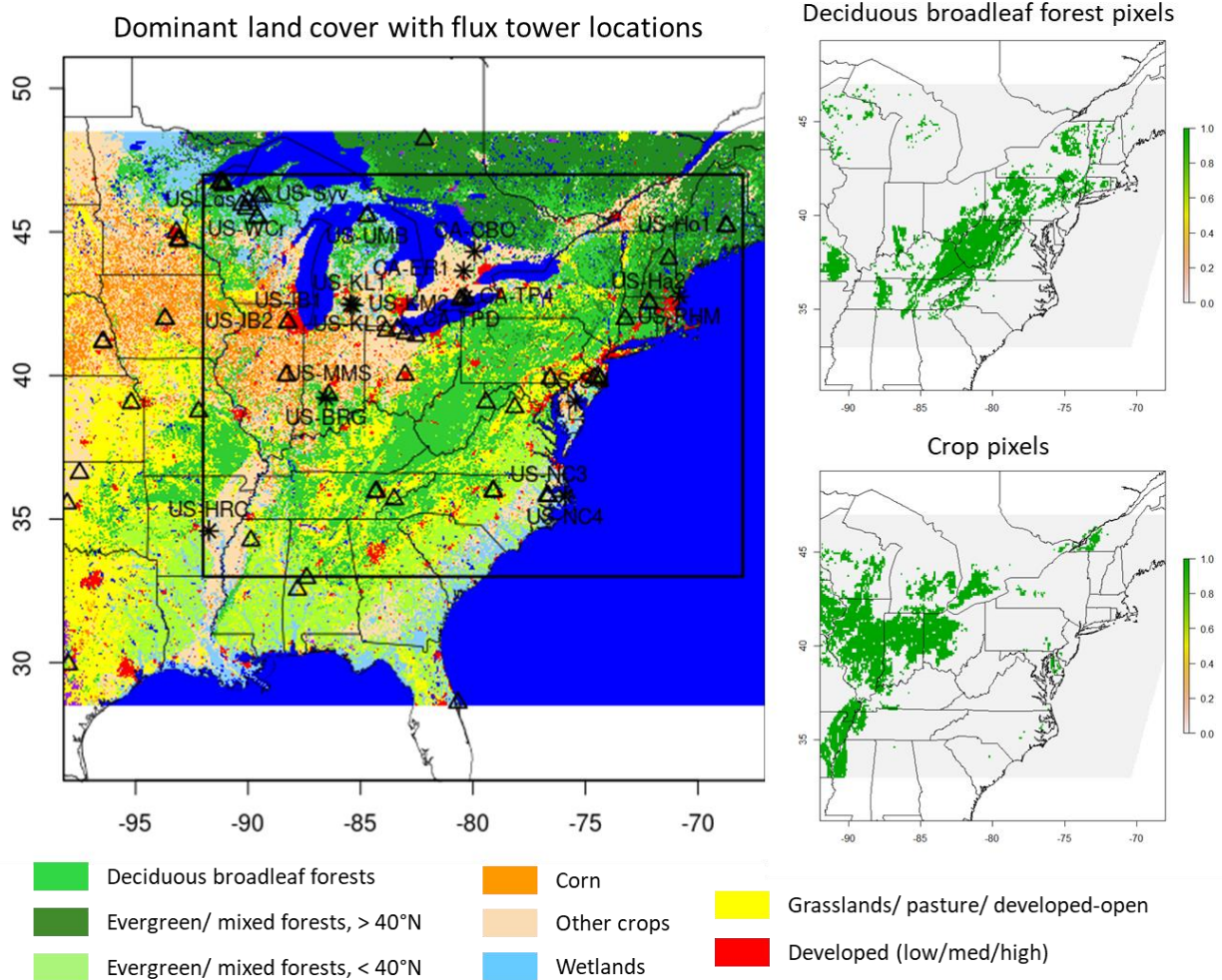


Figure 2: a) map of CO₂ observational towers and mean July 2017 afternoon atmospheric footprints (averaged across WRF-STILT and NAMS-STILT and summed across towers). The inner nests for the WRF simulation are shown in dark pink. (SNJ and SMT have no CO₂ observations in July 2017; therefore, their footprints are not included in the map.) b) and c) mean spatially integrated footprints in July 2017 as a function of hours back from receptor time for two towers: UNY (45 m inlet height) and MNC (213 m inlet height). Time series are averaged across all days in the month for each afternoon receptor hour. Receptor hours starting at 12 – 4 pm EST are shown with a thicker line width, although the expanded definition of “afternoon” in this study (as described in the supplemental material) allows for more hours with well-mixed conditions during summer months (shown with green shading). Other hours back in time are shaded to indicate day (yellow) or night (blue).

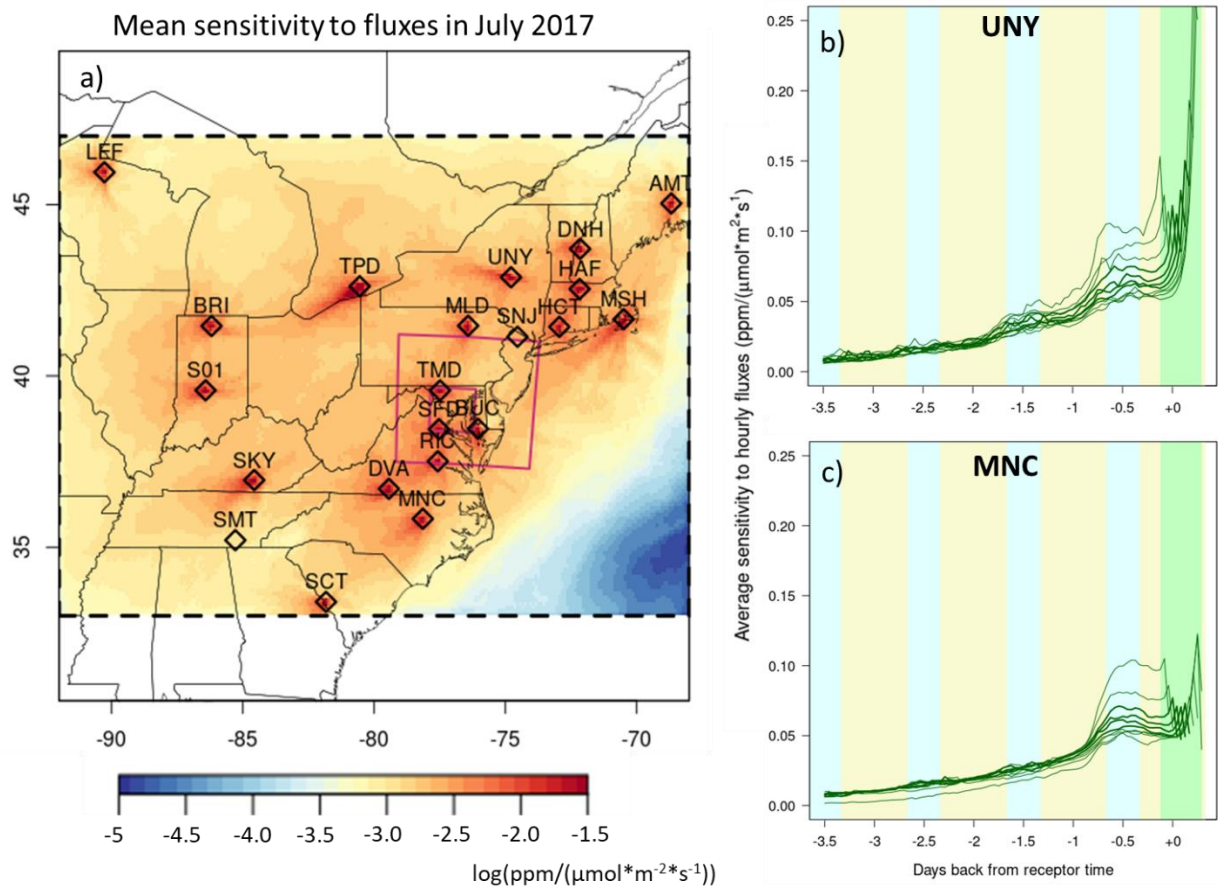


Figure 3: Atmospheric CO₂ observations across towers compared in four different ways: (a) total afternoon average CO₂ mole fraction for each tower across full year (in grey), with their average in red and background contribution from CT19 in blue, b) afternoon average biologic enhancements (using CT19 background) for each tower across full year (in grey), with difference in background conditions shown in orange, c) mean hourly diurnal cycle of biological enhancements with CT19 background conditions for each tower in January (grey) and the mean FF contribution across towers in gold, and d) the same as (c) but in July. For (c) and (d), afternoon hours have a thicker line width, with “afternoon” defined as described in the text. Red line indicates the spatial mean across towers in (a) and (b), and green for (c) and (d). Convolutions and background conditions are averaged across WRF-STILT and NAMS-STILT transport.

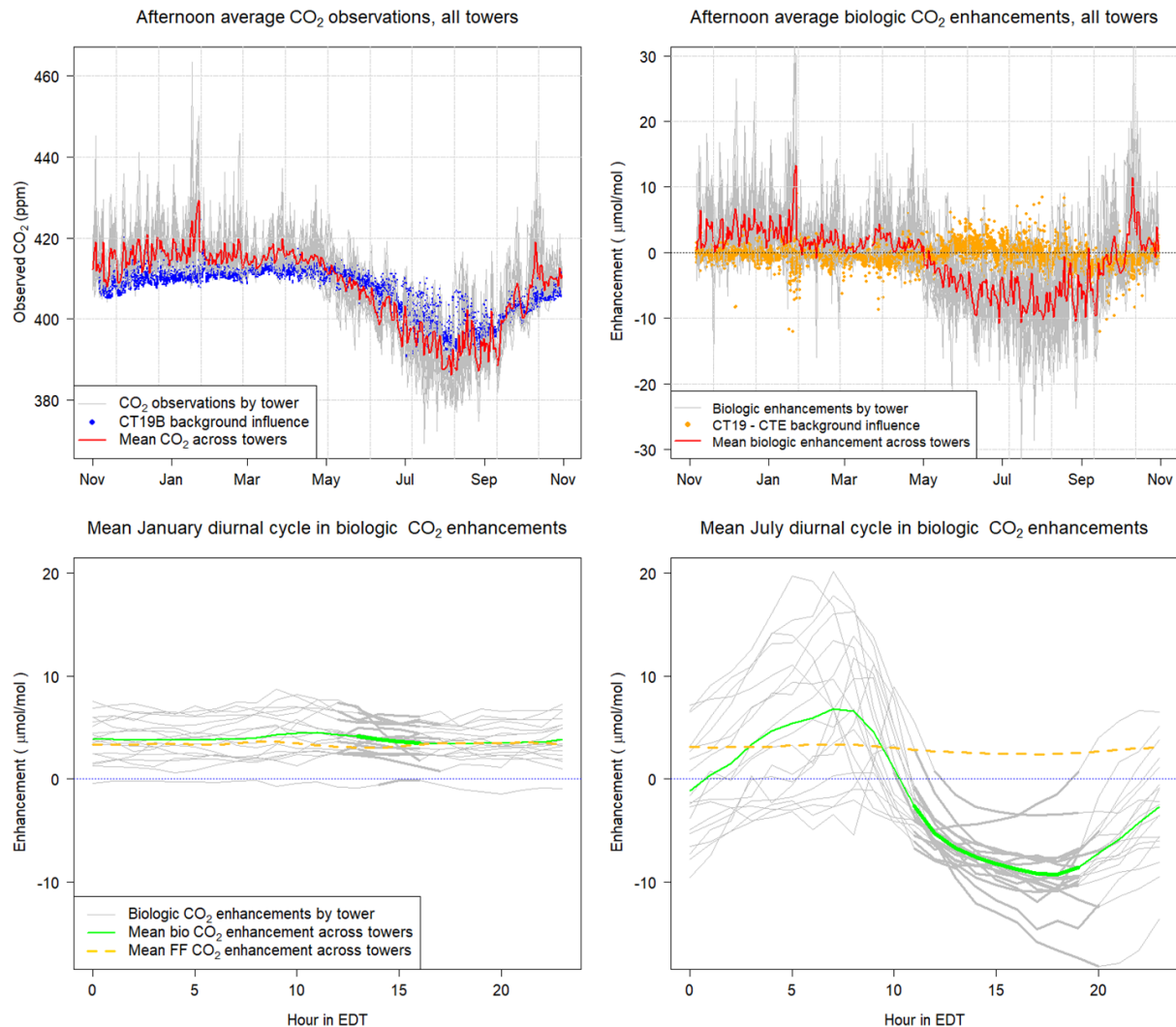


Figure 4: Scatter plots of observed air temperature vs. night-time average NEE for historical flux tower data used in the VPRM parameter optimization. The VPRM_{ann} model fit is shown in yellow, VPRM_{seas} in light green, and VPRM_{new} in dark green, with four lines for VPRM_{seas} corresponding to each season. Also shown are results from a linear regression model fit to just night-time NEE data (purple) for comparison. Results are shown for four PFT's (representing ~65% of total land cover in domain): deciduous broadleaf forests (27% + 5% urban), evergreen needleleaf/mixed forests >40°N (12%), maize crops (8%) and soybean/ other crops (13%). The NSC values (equivalent to the adjusted r^2 for VPRM_{new} and the linear regression model) are also shown to assess relative performance for each model and PFT.

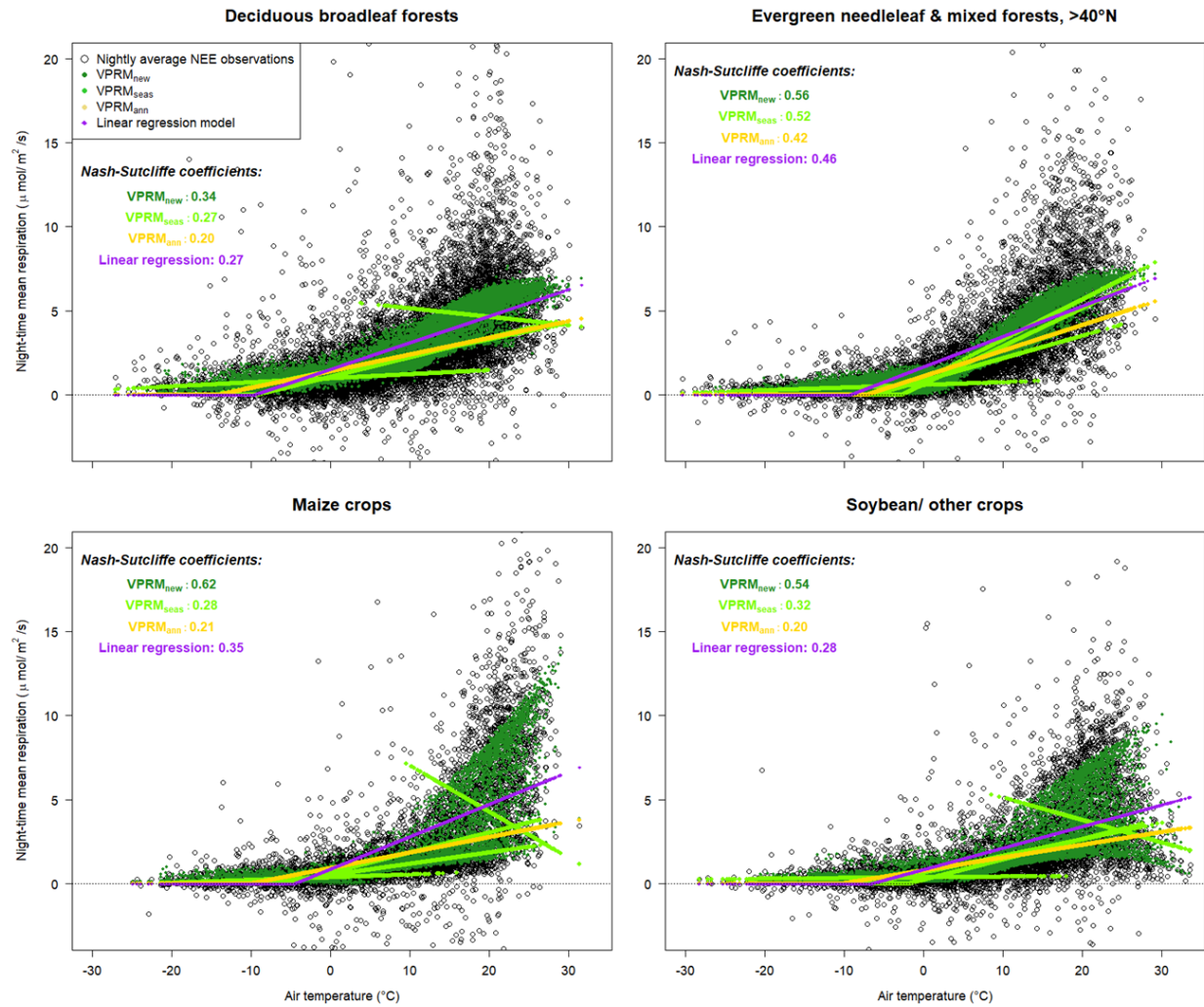


Figure 5: Mean 24-hour gridded GPP, ecosystem respiration (R_e) and NEE at 0.1° for SiB4, CASA and VPRM_{new} in winter months (December/ January/ February).

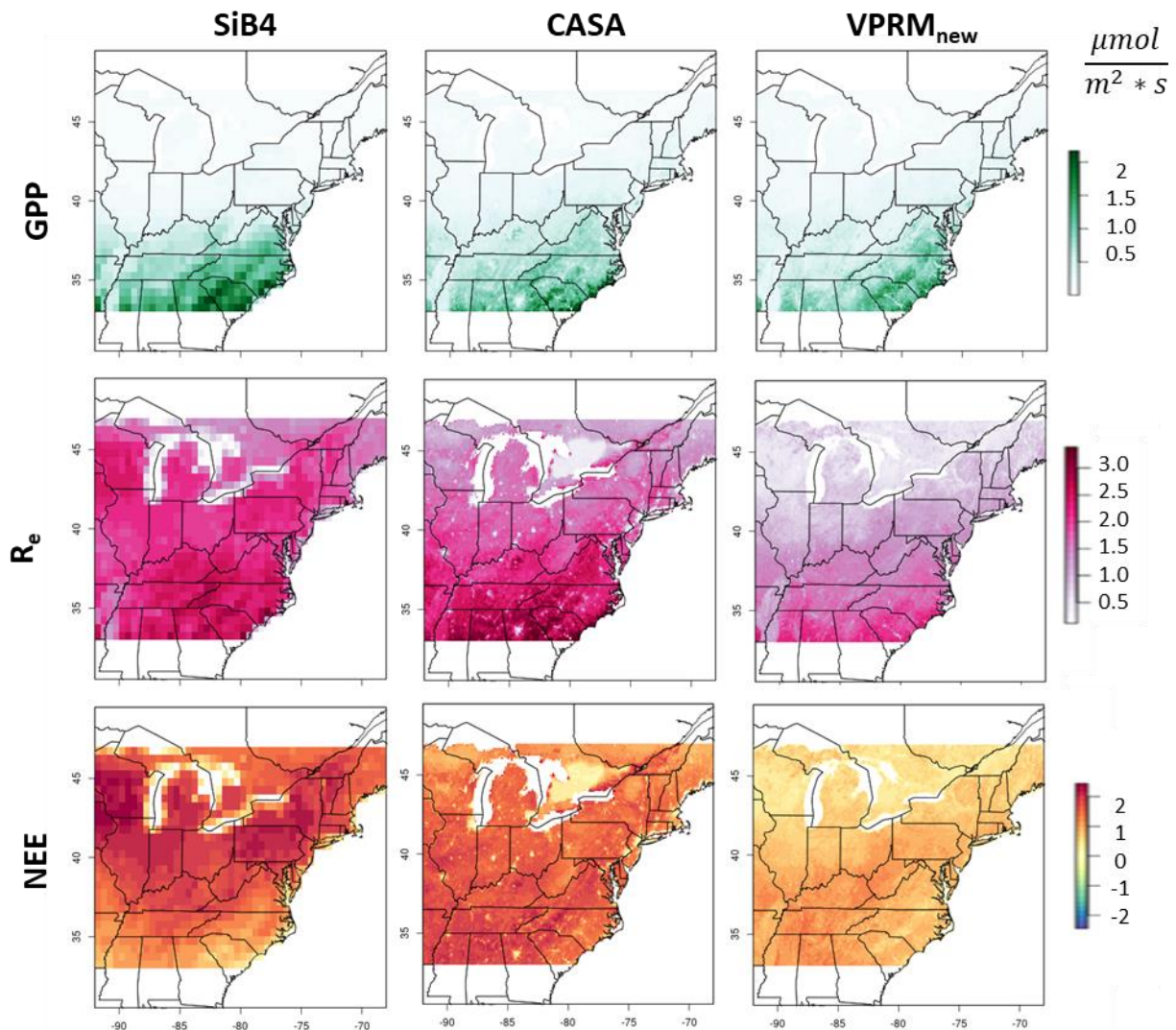


Figure 6: Mean 24-hour gridded GPP, ecosystem respiration (R_e) and NEE at 0.1° for SiB4, CASA and VPRM_{new} in spring months (March/ April/ May).

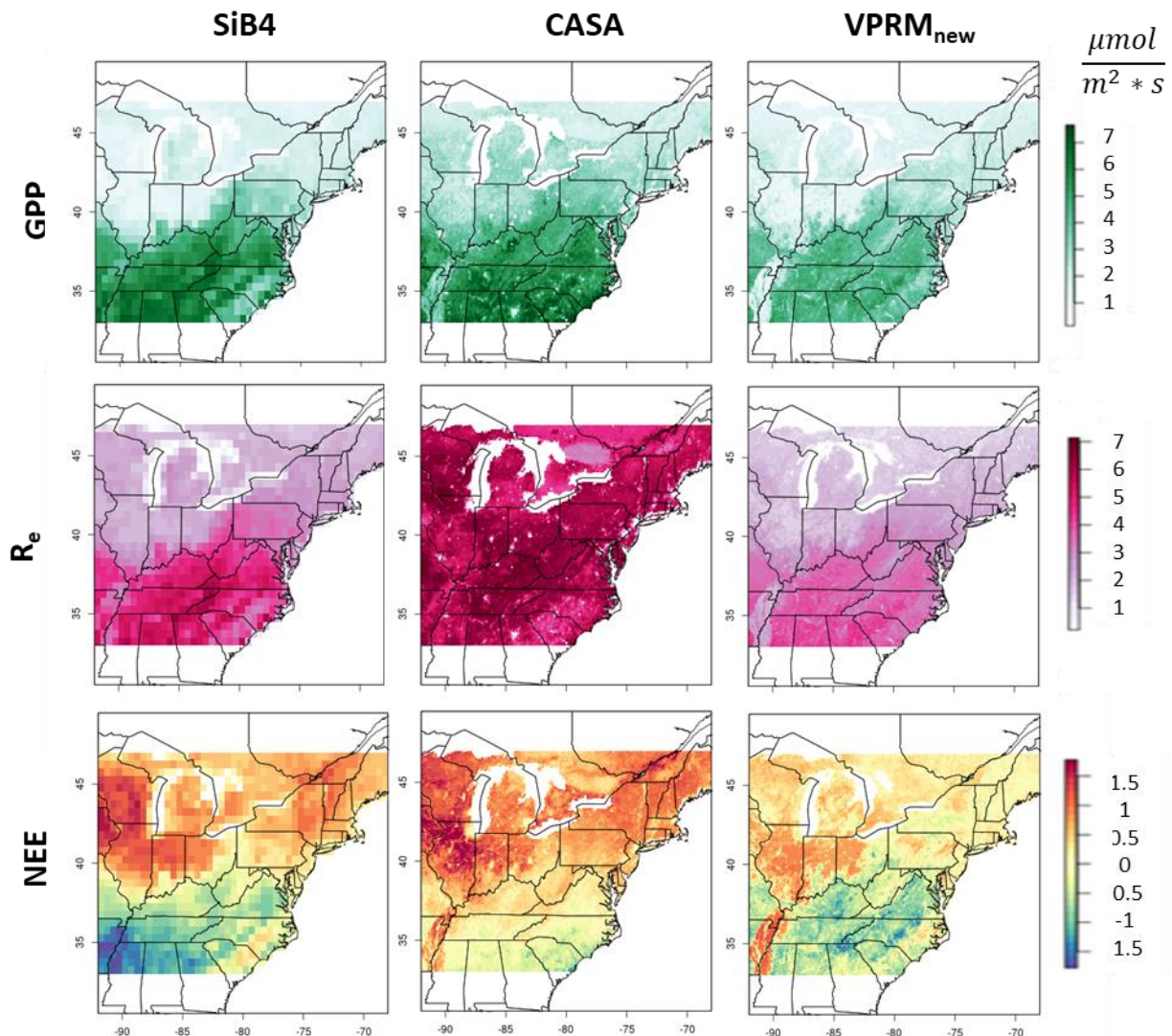


Figure 7: Mean 24-hour gridded GPP, ecosystem respiration (R_e) and NEE at 0.1° for SiB4, CASA and VPRM_{new} in summer months (June/ July/ August).

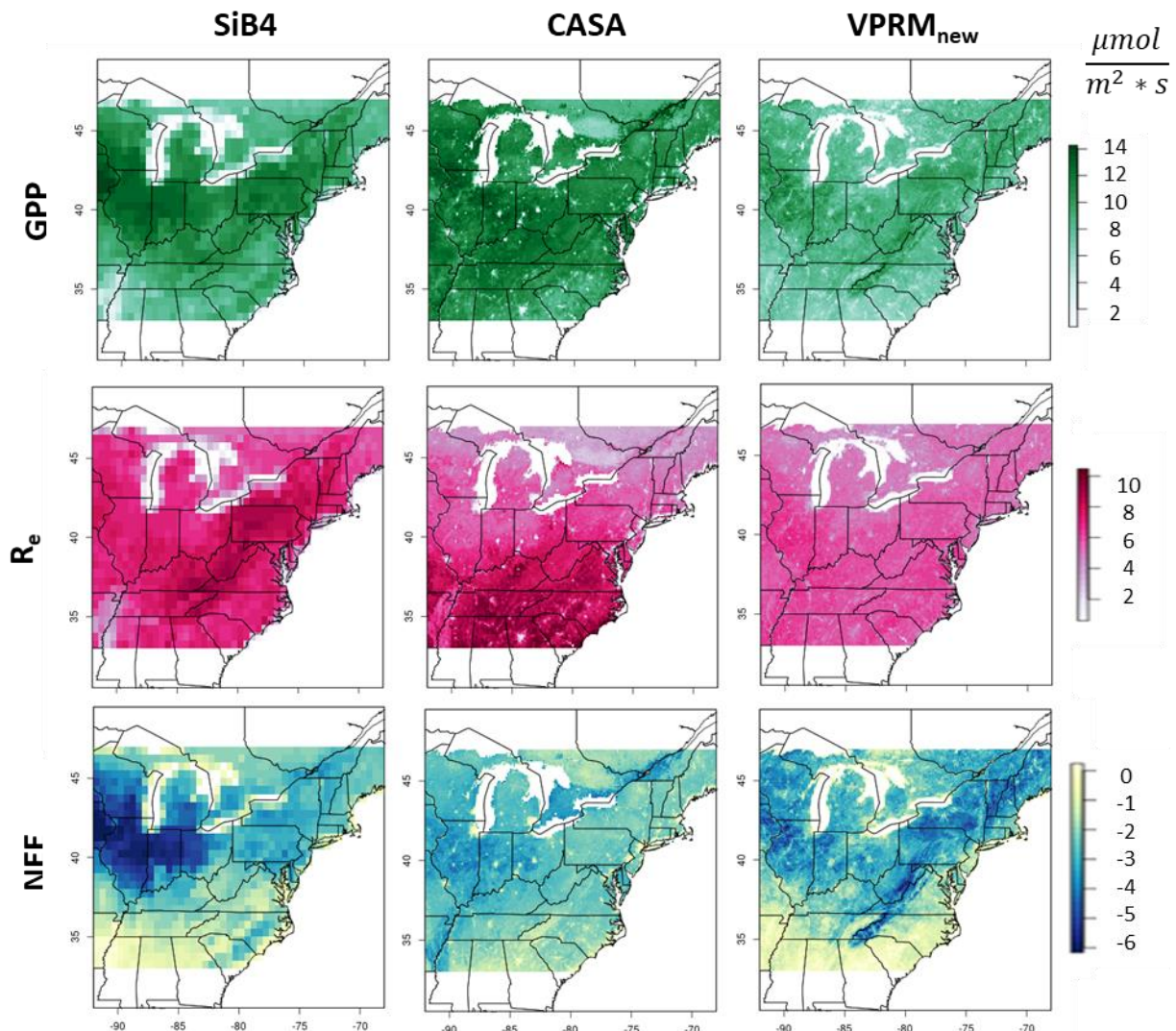


Figure 8: Mean 24-hour gridded GPP, ecosystem respiration (R_e) and NEE at 0.1° for SiB4, CASA and VPRM_{new} in fall months (September/ October/ November).

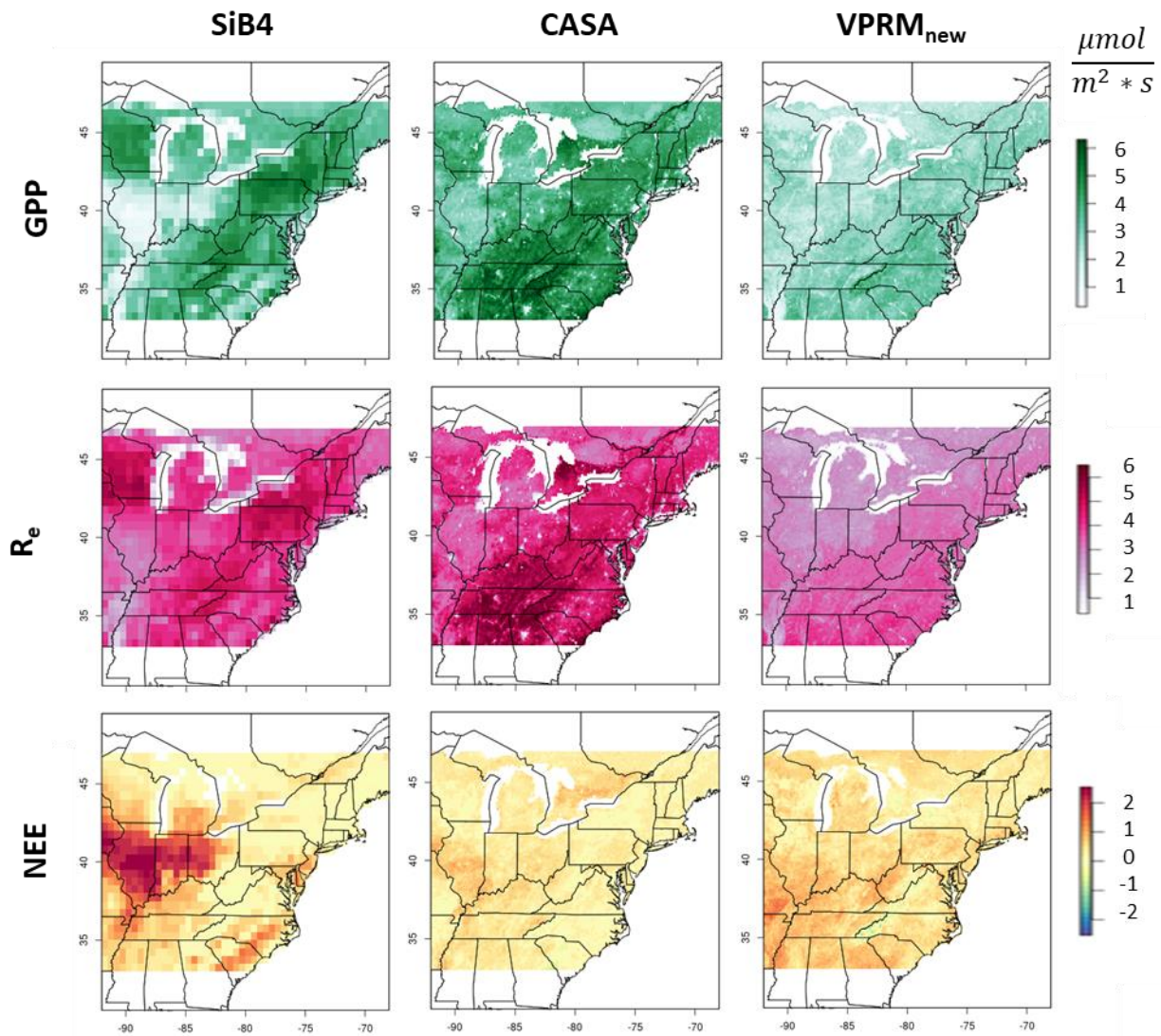


Figure 9: Seasonal cycle of weekly mean GPP, R_e & NEE fluxes, spatially aggregated across pixels with predominantly deciduous broadleaf forests (DBF, top row) and croplands (bottom row), as indicated in Figure 1. Annual means are shown with dashed lines.

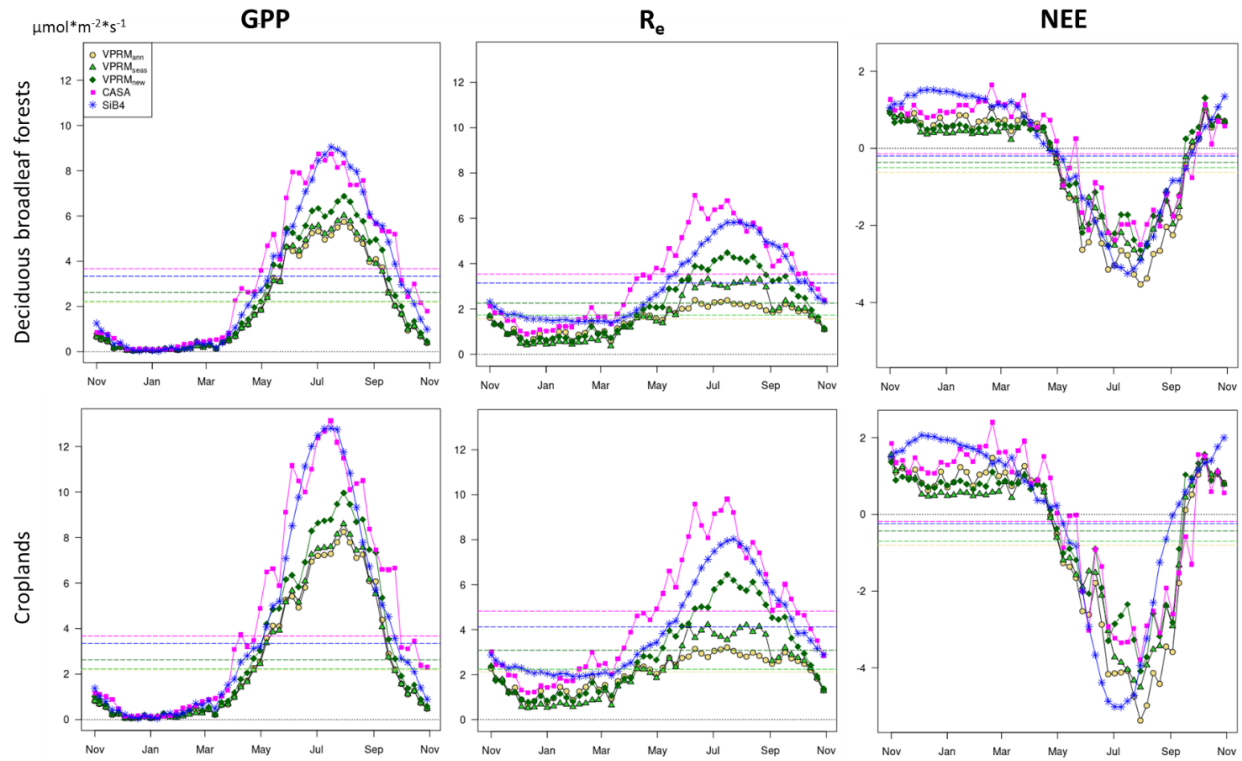


Figure 10: Comparison of VPRM_{new}, VPRM_{seas}, VPRM_{ann}, CASA and SiB4 to observed NEE at 22 flux towers in 2016/ 2017. Model output is extracted at flux tower locations at the 0.02° scale for VPRM, 500 m (or 5 km) for CASA and for the flux tower PFT in the SiB4 0.5° pixel. a) boxplot across towers of monthly mean biases (model – observations) for each model during nighttime hours. b) same as a), but for daytime hours. c) mean July NEE diurnal cycle comparing observations to models at the US-IB1 tower. d) same as c), but for the US-UMB tower. The 22 flux towers included in a) and b) are shown in Figure 1.

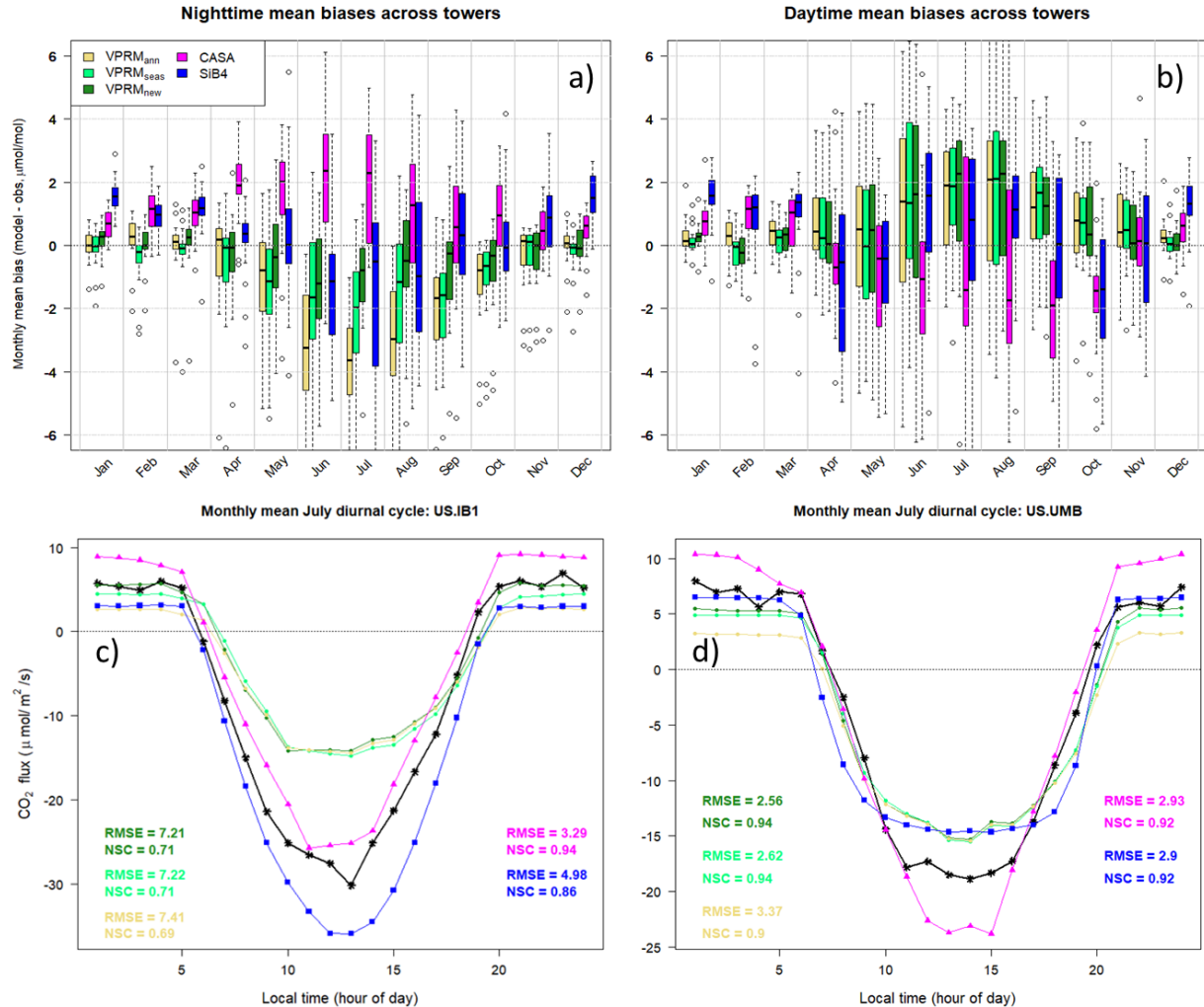


Figure 11: Weekly mean observed and simulated biological enhancements for VPRM_{new}, CASA and SiB4 at two [CO₂] towers: S01 in Indiana (44 % crops, 30 % forested within the footprint; left) and DNH in New Hampshire (63 % forested, 9 % crops within the footprint; right). The tables below show NSC and R²_a metrics comparing weekly mean enhancements from May to October and November to April, with the best performing biospheric model highlighted in red and bold. Enhancements are determined using average convolutions with WRF-STILT and NAMS-STILT transport, and with “optimal” monthly background conditions and Vulcan 3.0 + FFDAS fossil fuel emissions. The same figures using WRF-STILT and NAMS-STILT transport alone are shown in Figures S13 and S14.

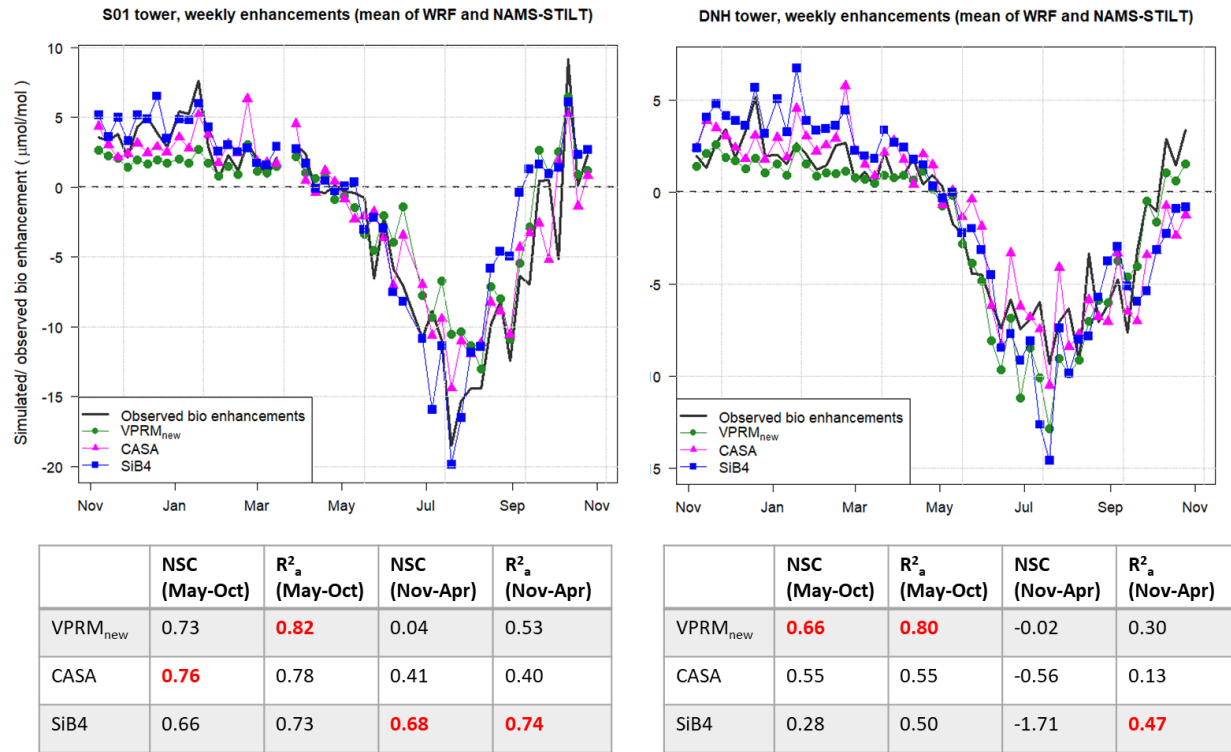
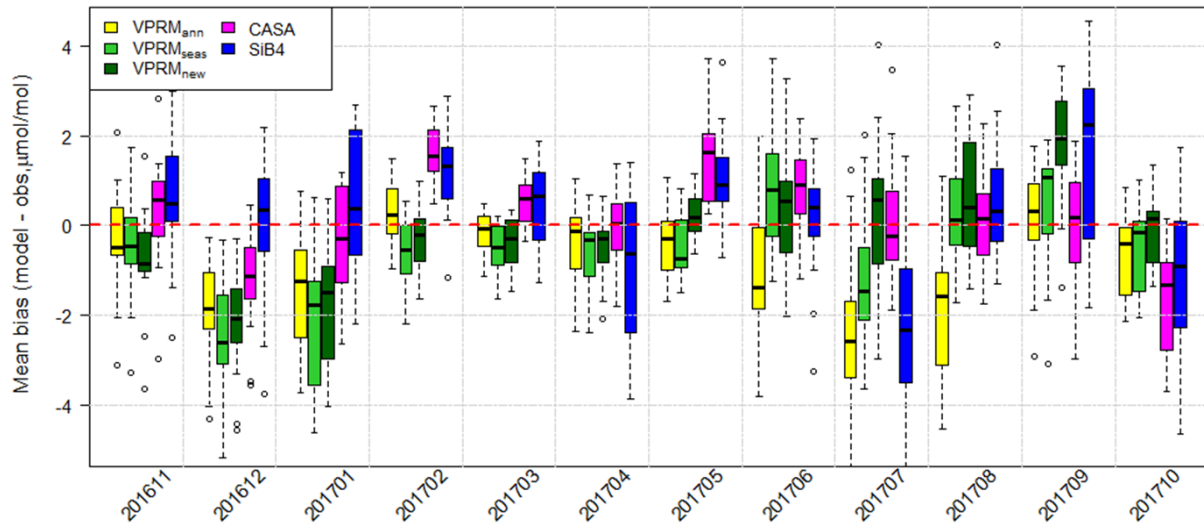


Figure 12: Boxplots across towers of monthly mean biases (simulated - observed biospheric CO₂ enhancements) from November 2016 to October 2017 for each biospheric model, using mean of WRF-STILT and NAMS-STILT convolutions, “optimal” background conditions and Vulcan 3.0 + FFDAS fossil fuel emissions. The table indicates the mean absolute error across towers for winter (Dec/Jan/Feb), spring (Mar/Apr/May), summer (Jun/Jul/Aug) and fall (Sep/Oct/Nov) months for each biospheric model, calculated using the monthly mean bias for each tower. Numbers in bold in the table indicate the least biased biospheric model(s) in each season (including models within 0.1 of the minimum). The same figures using WRF-STILT and NAMS-STILT transport alone are shown in Figure S15.



MAE across towers	VPRM _{ann}	VPRM _{seas}	VPRM _{new}	CASA	SiB4
Dec-Feb	1.47	1.94	1.70	1.11	1.25
Mar-May	0.57	0.71	0.61	0.97	1.19
Jun-Aug	1.73	1.20	1.03	1.19	1.64
Sep-Nov	1.25	1.00	1.30	1.20	1.67

Figure 13: Monthly Nash-Sutcliffe coefficients (left panel) and adjusted R^2 (right panel) comparing convolutions from each biospheric model to observed hourly biologic enhancements across all towers. Convolutions using WRF-STILT and NAMS-STILT transport are averaged, and Vulcan3.0 (+FFDAS in Canada) fossil fuel emissions and “optimal” monthly background conditions are used for all comparisons. The same plots using WRF-STILT or NAMS-STILT transport alone are shown in the supplemental material in Figure S17.

